

A Non-Gray Theory of Extrasolar Giant Planets and Brown Dwarfs

A. Burrows¹, M. Marley², W.B. Hubbard³, J.I. Lunine³, T. Guillot⁴, D. Saumon⁵, R.
Freedman⁶, D. Sudarsky¹, and C. Sharp¹

Received _____; accepted _____

February 1, 2008

¹Department of Astronomy and Steward Observatory, University of Arizona, Tucson, AZ 85721

²Department of Astronomy, New Mexico State University, Box 30001/Dept. 4500, Las Cruces NM 88003

³Lunar and Planetary Laboratory, University of Arizona, Tucson, AZ 85721

⁴Department of Meteorology, University of Reading, P.O. Box 239, Whiteknights, Reading RG6 6AU, United Kingdom

⁵Department of Physics and Astronomy, Vanderbilt University, Nashville, TN 37235

⁶Sterling Software, NASA Ames Research Center, Moffett Field CA 94035

ABSTRACT

We present the results of a new series of non-gray calculations of the atmospheres, spectra, colors, and evolution of extrasolar giant planets (EGPs) and brown dwarfs for effective temperatures below 1300 K. This theory encompasses most of the mass/age parameter space occupied by substellar objects and is the first spectral study down to 100 K. These calculations are in aid of the multitude of searches being conducted or planned around the world for giant planets and brown dwarfs and reveal the exotic nature of the class. Generically, absorption by H_2 at longer wavelengths and H_2O opacity windows at shorter wavelengths conspire to redistribute flux blueward. Below 1200 K, methane is the dominant carbon bearing molecule and is a universal diagnostic feature of EGP and brown dwarf spectra. We find that the primary bands in which to search are Z ($\sim 1.05 \mu\text{m}$), J ($\sim 1.2 \mu\text{m}$), H ($\sim 1.6 \mu\text{m}$), K ($\sim 2.2 \mu\text{m}$), M ($\sim 5 \mu\text{m}$), and N ($\sim 10 \mu\text{m}$), that enhancements of the emergent flux over blackbody values, in particular in the near infrared, can be by *many* orders of magnitude, and that the infrared colors of EGPs and brown dwarfs are much bluer than previously believed. In particular, relative to J and H , the K band flux is reduced by CH_4 and H_2 absorption. Furthermore, we derive that for T_{eff} s below 1200 K most or all true metals are sequestered below the photosphere, that an interior radiative zone is a generic feature of substellar objects, and that clouds of H_2O and NH_3 are formed for T_{eff} s below ~ 400 K and ~ 200 K, respectively. This study is done for solar-metallicity objects in isolation and does not include the effects of stellar insolation. Nevertheless, it is a comprehensive attempt to bridge the gap between the planetary and stellar realms and to develop a non-gray theory of objects from $0.3 M_{\text{J}}$ (“saturn”) to $70 M_{\text{J}}$ ($\sim 0.07 M_{\odot}$). We find that the detection ranges for brown dwarf/EGP

discovery of both ground– and space–based telescopes are larger than previously estimated.

Subject headings: extrasolar giant planets, brown dwarfs, non–gray spectral synthesis, atmospheres

1. Introduction

After years of slow progress and ambiguous, but tantalizing, observations of objects in the field and in young clusters, the study of brown dwarfs via reflex stellar motion, filter photometry, and spectroscopy has finally come into its own. The direct detection of Gl229B (Oppenheimer *et al.* 1995; Nakajima *et al.* 1995; Matthews *et al.* 1996; Geballe *et al.* 1996; Marley *et al.* 1996; Allard *et al.* 1996; Tsuji *et al.* 1996) was a watershed because Gl229B displays methane spectral features and low surface fluxes that are unique to objects with effective temperatures (in this case, $T_{\text{eff}} \sim 950$ K) below those at the solar-metallicity main sequence edge (~ 1750 K, Burrows *et al.* 1993). In addition, the almost complete absence of spectral signatures of metal oxides and hydrides (such as TiO, VO, FeH, and CaH) is in keeping with theoretical predictions that these species are depleted in the atmospheres of all but the youngest (hence, hottest) substellar objects and are sequestered in condensed form below the photosphere (Lunine *et al.* 1989; Marley *et al.* 1996). This remarkable convergence between theory and observation should not obscure the fact that the study of the atmospheres, spectra, colors, and evolution of substellar objects is still in its infancy. Though predictions of luminosity, T_{eff} , and radius evolution versus mass and composition have been available for almost a decade (Nelson *et al.* 1985; D’Antona & Mazzitelli 1985; Burrows, Hubbard, & Lunine 1989; Dorman *et al.* 1989; Stevenson 1991; Stringfellow 1991; Burrows *et al.* 1993) and predictions for the colors and spectra of hot ($\gtrsim 2000$ K), young brown dwarfs have been available for a few years (Allard & Hauschildt 1995), to date there has been no *complete* theory of the evolution of the colors, spectra, and structure of brown dwarfs with temperatures below ~ 1300 K. This is true despite the fact that, for most of the mass–age space occupied by brown dwarfs in the galaxy, T_{eff} is indeed below 1300 K. To remedy this situation, we here present the first non-gray theory of the evolution, spectra, and colors of brown dwarfs down to T_{eff} s of 100 K.

This sweep of T_{eff} s and the effective physical equivalence between equal-mass extrasolar giant planets (EGPs) and brown dwarfs allows our theory to apply, without modification, to EGPs as well. It is sensible to distinguish EGPs and brown dwarfs on the basis of their origins: brown dwarfs form like stars, but are too light to burn hydrogen stably on the main sequence, and EGPs form out of protoplanetary disks by accretion. The different birth paths no doubt lead to different metallicities, rotation rates, and orbital characteristics, and in the giant planet case to the presence of an “ice/rock” core (Podolak, Hubbard, & Pollard 1993). However, in the main it is not the origin, but the mass, composition, age, and proximity of a hydrogen-dominated object to a star that determines its spectral signatures and evolution. An object’s pedigree is not an obvious observable.

We have already published a general theory of extrasolar giant planets with masses from $0.3 M_J$ to $15 M_J$, where M_J denotes a Jupiter mass ($\sim 0.001 M_\odot$) (Burrows *et al.* 1995; Saumon *et al.* 1996; Guillot *et al.* 1996). When we published these EGP models, no such objects had been identified. Now, Doppler spectroscopy alone has revealed about 20 objects in the giant planet/brown dwarf regime, including companions to τ Boo, 51 Peg, v And, 55 Cnc, ρ CrB, 70 Vir, 16 Cyg, and 47 UMa (Butler *et al.* 1997; Cochran *et al.* 1997; Marcy & Butler 1996; Butler & Marcy 1996; Mayor & Queloz 1995; Latham *et al.* 1989). However, our old theory assumed that EGPs emit like blackbodies. While this assumption is not bad for some wavelength stretches in the mid-infrared, it can be spectacularly off in bands of interest for direct detection. The Gl229B campaign taught us that. The non-gray theory we develop in this paper encompasses masses from $0.3 M_J$ to $70 M_J^\dagger$ and is in aid of the multitude of direct searches for substellar objects, be they “planets” or brown dwarfs, upon which the world’s astronomical community has now collectively embarked (TOPS and ExNPS reports; Leger *et al.* 1993). In order to maintain a reasonable focus, we limit

[†] For a $70 M_J$ brown dwarf, $T_{\text{eff}} < 1300$ K for $\gtrsim 4$ Gyr.

ourselves to solar-metallicity (Anders & Grevesse 1989) objects in isolation and ignore the effects of stellar insolation (Guillot *et al.* 1996). A subsequent paper will address the consequences of proximity to a central star and of varying metallicity.

In §2, we describe our calculational techniques and the opacity and thermodynamic data that we used. Section 3 covers the physics of the atmospheres of brown dwarfs and EGPs and includes a discussion of temperature/pressure/composition profiles and the location of convective and radiative zones. In §4, we describe the evolution of objects with masses from $0.3 M_J$ to $200 M_J$, from saturns to M dwarfs, and provide a global view of the giant planet/brown dwarf/M dwarf model continuum. Section 5 contains a comprehensive discussion of the near- and mid-infrared spectra of EGPs and brown dwarfs as a function of mass and age, as well as T_{eff} and gravity. Our major results are to be found in this section. Section 6 presents the IR colors and magnitudes from the J through the N bands and demonstrates just how unlike blackbodies these objects can be. Search and discovery techniques using Doppler spectroscopy, astrometry, transits, and microlensing are rapidly maturing, but it is only via direct photometric and spectroscopic characterization that substellar objects will really be understood. In §7, we summarize the salient features of the non-gray theory and list some of the ground- and space-based telescopes and searches for which it should prove useful.

2. Input Physics

The ingredients for a theory of EGPs and brown dwarfs include (1) equations of state for metallic hydrogen/helium mixtures and molecular atmospheres, (2) chemical equilibrium codes and thermodynamic data to determine the molecular fractions, (3) scattering and absorption opacities for the dominant chemical species, (4) an atmosphere code to calculate temperature/pressure profiles and to identify the radiative and convective zones, (5) an

algorithm for converting a grid of atmospheres into boundary conditions for evolutionary calculations, (6) a Henyey code, and (7) a radiative transfer code to provide emergent spectra. In principle, the calculation of the atmosphere, involving as it does radiative transfer, and the calculation of the emergent spectrum are done together. However, as long as the thermal profiles obtained with the atmosphere code are accurate, one can employ these profiles, but with another more accurate and higher-resolution transfer scheme, to calculate emergent spectra. Though we use the k-coefficient method to calculate the atmosphere profiles, we are free to employ other radiative transfer schemes to obtain spectra.

In the evolutionary calculations, we use the Saumon & Chabrier (1991, 1992) equation of state in the metallic and high-density molecular regimes. For solar metallicity, near and above brown dwarf/EGP photospheres, throughout most of their lives the dominant equilibrium form of carbon is CH_4 , not CO (Fegley & Lodders 1996), that of oxygen is H_2O , and that of nitrogen is either N_2 or NH_3 , depending upon T_{eff} . Hydrogen is predominantly in the form of H_2 . Silicates and metals are found at high optical depths and temperatures. Clouds of NH_3 and H_2O can form for T_{eff} s below ~ 200 K and ~ 400 K, respectively. While for this new model suite we have precipitated species according to their condensation curves, we have not consistently incorporated the effects of the associated clouds. If a species has condensed, it is left at its saturated vapor pressure. Though the proper inclusion of the radiative transfer effects of clouds is deferred to a later work, in §2.6 & §3 we discuss the basic physics of such clouds for T_{eff} s between 100 K and 1300 K (see also Lunine *et al.* 1989) and speculate on their role in spectrum formation.

2.1. Opacities

Water is an important source of opacity in EGPs and brown dwarfs, particularly when the many lines that originate from highly excited energy levels are considered. A series of databases have recently become available that are based on theoretical calculations that employ a variety of quantum mechanical methods (Polyansky, Jensen, & Tennyson 1994; Wattson & Rothman 1992; Partridge & Schwenke 1997). In particular, Partridge & Schwenke have calculated the potential energy surface and dipole moment function using an ab initio method. This energy surface was empirically adjusted to improve the fit between predictions and the HITRAN 92 database (Rothman *et al.* 1992) for $J \lesssim 5$. The overall accuracy in wavenumber and intensity is good and the data have already been used to identify previously unidentified sunspot lines as water lines (Carbon & Goorvitch 1994). The 10, 25, 50, 75, and 90 percentiles of the errors in the line positions as compared to HITRAN are: -0.11, -0.04, -0.01, 0.02, and 0.07 cm^{-1} . This database allows the inclusion of many predicted lines that are unobserved in the lab and only become important at higher temperatures, since they arise from highly excited levels. This can be particularly important in opacity windows, *i.e.*, regions where the water opacity reaches a local minimum, but where many weak, high-excitation lines may occur. Depending upon the temperature of the layer, and the assumed abundance of water, well over 2.0×10^8 lines could be required for a calculation at the highest temperatures, while far fewer lines are needed at lower temperatures. We use this new Partridge & Schwenke H₂O database. (Note that the model published by Marley *et al.* (1996) used an earlier version of the Schwenke data with fewer lines.)

For other than H₂O, we used databases that go beyond what is available in the HITRAN database (Rothman *et al.* 1997). The limitations of HITRAN are a consequence of the cutoff in line strength that is imposed at a temperature of 296 K. Weaker lines are

excluded by this cutoff, though they may become much stronger as the temperature climbs to well above 300 K. In addition, in HITRAN lines whose analysis is lower in quality may have been excluded. Since in our application we are interested in the total opacity only over fairly broad regions in wavenumber, we can accept lines whose positions and strengths may not be known with the highest precision. This makes available databases with far more lines than HITRAN. The GEISA database (Husson *et al.* 1997) can also be a source of additional lines, as its line strength cutoff is lower than that of HITRAN. Additional lines have been obtained from theoretical calculations (Tyuterev *et al.* 1994; Goorvitch 1994; Tipping 1990; Wattson & Rothman 1992) and from other researchers prior to publication (L. R. Brown, private communication). This has resulted in databases for CH₄ and CH₃D of 1.9×10^6 lines, for CO of 99,000 lines, for NH₃ of 11,400 lines, for PH₃ of 11,240 lines, and for H₂S of 179,000 lines.

Modeled continuum opacity sources include H[−] and H₂[−] opacity and collision-induced absorption (CIA) of H₂ and helium (Borysow & Frommhold 1990; Zheng & Borysow 1995). The latter is a direct function of pressure and a major process in EGP/brown dwarf atmospheres. We employed the formulation of Rages *et al.* (1991) for Rayleigh scattering, important at shorter wavelengths.

2.2. Line Profiles

For our calculations, when the data are available, the line widths for the various molecules are assumed to be due to H₂ or H₂ + He broadening. Currently, such data are available for H₂O (Brown & Plymate 1996; Gamache, Lynch, & Brown 1996), CO (Bulanin *et al.* 1984; Lemoal & Severin 1986), CH₄ (Margolis 1993,1996; L. R. Brown, private communication), PH₃ (Levy, Lacome, & Tarrago 1994), and NH₃ (Brown & Peterson 1994). These data were derived from laboratory measurements, and the width for each line was

derived from a fit to the available data as a function of the value of J and the other relevant rotational quantum numbers. Because these measurements typically cover only one or more vibrational bands, it is necessary to assume that any vibrational dependence of the widths is very small, since the same fit is used for all bands. For other species it is necessary to use the available N_2 widths, under the assumption that the broadening due to H_2 is larger than that due to N_2 , because of the difference in quadrupole moments. This is still quite uncertain and may vary from species to species.

2.3. Calculation of the Atmosphere Structures and Spectra

We construct model atmospheres employing an approach similar to that used to derive temperature profiles for the outer planets (Marley *et al.* 1997) and Titan (McKay *et al.* 1989). The model consists of a series of up to 60 homogeneous plane-parallel layers. The bottom of the lowermost layer is placed at a depth of up to 300 bars, the top of the uppermost at 0.5 mbars. Levels, which separate layers, are spaced approximately evenly in $\log P$. The current model considers 101 spectral intervals from $0.87\ \mu\text{m}$ to $2.5\ \text{cm}$.

A trial temperature profile is adjusted until the entire atmosphere is in radiative equilibrium. The model is judged to be in radiative equilibrium when the temperature profile results in zero net flux across each level in the radiative region of the atmosphere. Layers in which the radiative lapse rate exceeds the adiabatic lapse rate are then deemed convective. The lapse rate is adjusted only one layer at a time and a new radiative-convective equilibrium profile is computed after the lapse rate in each layer is adjusted. This approach allows for the presence of multiple convection zones and works very well for the solar Jovian planets (Marley *et al.* 1997). The scaling arguments of Ingersoll & Pollard (1982) suggest that the fractional difference between the actual temperature profile and an adiabat is less than 10^{-4} for Jovian atmospheres.

Fluxes are computed using the two-stream source function technique (Toon *et al.* 1989). The intensity is integrated over five angular Gauss points in each hemisphere. This technique is rapid and is well suited for application to inhomogeneous, multiple-scattering atmospheres. Toon *et al.* discuss the accuracy of this approach for a variety of scattering and non-scattering cases. For the case of no scattering, they found layer emissivities to agree with an exact calculation to better than 1% over a three decade range of layer optical depths.

2.4. The k-coefficient Method

The k-coefficient method (Goody *et al.* 1989; Lacis & Oinas 1991) is widely used in planetary atmosphere modeling. This is not the ODF technique (Saxner & Gustafsson 1984) and gives excellent agreement with full line-by-line computations of atmospheric transmission. Typical errors are between 1 and 10% (Grossman & Grant 1992,1994a,1994b).

After we perform the line-by-line calculations for each individual molecule, the resulting opacity files are put on a common frequency scale. Then, they are combined into one file for the total opacity using the appropriate mixing ratios for each molecule. The abundance of the various constituents is determined by a chemical equilibrium calculation and condensation (§2.5 & §2.6). At temperatures below the condensation point of a given constituent, the abundance is set equal to the saturation vapor pressure. In the k-coefficient method, this summed file is then broken up into a large number (~ 100) of frequency blocks covering the entire spectrum. The creation of the block structure allows one to avoid solving the transfer equation at a very large number of individual frequency points (Goody *et al.* 1989).

One constructs a distribution function of all the opacities within each frequency

block. This technique takes all the opacities (at each wavenumber) from the line-by-line calculation, sorts them according to value (independent of wavenumber), and places them in logarithmically-spaced bins. Note that this destroys the relationship between a particular value of the opacity and the wavenumber where it occurred. This distribution (number of points that fall in each bin versus opacity) is then normalized and converted into a cumulative distribution. The distribution is now the cumulative number of points at each bin versus the opacity of that bin. After the proper normalization, this now gives the cumulative probability versus opacity, *i.e.* the probability that an opacity is less than or equal to a given value. This distribution is then inverted using interpolation to give the final cumulative probability distribution. The abscissa is now the probability normalized to run from 0 to 1.0 and the ordinate is opacity and runs from the minimum to the maximum value of the opacity within the window.

Because the final distribution is now uniform in probability space, it is possible to integrate this distribution to find the total opacity in each window. We perform this integration by extracting values at appropriate Gauss points. These values, sometimes called correlated k 's, can be used with the appropriate Gauss weights to represent the total opacity in a given window.

All molecular absorption is treated within each spectral interval by a weighted sum of exponentials. The transmission, T , as a function of absorber column mass, u , within a layer for a given spectral interval is expressed as

$$T(u) = \sum_i w_i e^{-k_i u} \quad (1)$$

where the w_i are weights and the k_i are equivalent monochromatic absorption coefficients.

Within each spectral interval the equation of radiative transfer is solved eight times as a monochromatic equation of transfer, once for each term in the expansion in eq. (1), with the Rayleigh optical properties identical for each of the computations. The fluxes thus

obtained are then summed, with the terms weighted by the w_i , to obtain the total flux in the spectral interval.

The accuracy of the approach is controlled by the width of the model spectral intervals and the number of Gauss points used. To improve the sensitivity to small fractions of very strong lines in a given spectral interval, we employ a double Gaussian quadrature. The first four Gauss points provide for the integral over the weakest 88% of the lines. The remaining four points take the integration over the remaining probability interval. Accuracy can be compromised if the spectral shape of the molecular opacity within a given interval changes with depth in the model, usually because of conversion of one species to another. Thus, we have carefully chosen the individual spectral intervals to minimize such effects. Experimentation with the current spectral intervals reveals that computed temperature profiles are not sensitive to a further increase in their number.

During model runs, the k -coefficients at an arbitrary temperature–pressure point are computed by interpolation within the k -coefficient grid. Opacities are interpolated in $\log P$ - $1/T$ space to follow the variation of constituents along the vapor pressure curve.

2.5. Chemical Equilibrium Calculations

For this paper, the chemical equilibrium calculations were performed with the ATLAS code and data from Kurucz (1970). The Kurucz reaction constants are inaccurate at low temperatures, but, fortunately, the $\text{NH}_3 \rightarrow \text{N}_2$ and $\text{CH}_4 \rightarrow \text{CO}$ conversions that occur in EGPs and brown dwarfs do so in regions of $T - P$ space for which the Kurucz reaction constants are accurate. Condensation of CH_4 , NH_3 , H_2O , Fe, and MgSiO_3 was included using data from various sources, including Eisenberg & Kauzmann (1969), the Handbook of Chemistry and Physics (1993), and Lange’s Handbook of Chemistry (1979). Following

Fegley & Lodders (1994, 1996), we assumed that Al, Ca, Ti and V were removed either by condensation or were dissolved in silicate grains at about the MgSiO_3 condensation temperature. These atoms are important because they lead to molecules that are strong light absorbers, such as TiO and VO. However, they have not been detected in the giant planets of our solar system and shouldn't be present in relatively cool objects such as the brown dwarf Gl229B (Marley *et al.* 1996). Our results are in excellent agreement with those of Fegley & Lodders (1994, 1996).

2.6. Condensation Processes

The principal effect of cloud formation is the removal of molecular species from the gas phase into the solid or liquid phase. For a single component system that does not interact chemically with other species (*i.e.*, water) cloud formation occurs at a pressure level (“cloud base”) where the partial pressure of the gaseous species just exceeds its saturation vapor pressure. The saturation vapor pressure is given approximately by the Clausius–Clapeyron relationship, $P = Be^{-A/T}$, where B and A are weak functions of temperature. A is the latent heat of condensation (per mole) divided by the universal gas constant. At lower pressures (higher altitudes) in the atmosphere, the abundance of the gas phase species drops off in this inverse–exponential fashion. Since $A/T > 1$, the falloff is steep and the gaseous species does not contribute to the emergent spectral distribution at pressures much above the cloud base.

There are several complications to the above simple picture. The first is supersaturation. Because the radius of curvature of cloud particles or droplets adds an additional surface energy to the condensed phase, the cloud base is usually elevated above the pressure level at which the ratio of partial pressure to saturation vapor pressure is unity (this is the supersaturation ratio). In the case of terrestrial clouds, the threshold ratio may be

1.2; in certain cold environments lacking particulates to serve as nucleation sites, the value may be as high as 2 (such as in Neptune; Moses, Allen, & Yung 1992). Because of the high temperatures at the unity optical depth level in objects such as Gl229B, we ignore supersaturation; variations of a few tens of percent in the supersaturation are not discernable in its spectra.

The second complication is that for most condensable species the temperature variation of A cannot be ignored in two cases: near the liquid–vapor critical point, and over large ranges of temperature. Because our models span a large temperature range, this is a concern for the major cloud–forming species, in particular water. For water, we use multi–term polynomial and exponential fits for the liquid and solid phases from Eisenberg & Kauzmann (1969). These are suitable for temperatures from well below the ice point to the critical temperature.

The third complication is that many cloud–forming elements are not incorporated in the same molecular species in the gaseous and condensed phases, but instead a chemical reaction occurs associated with the condensation process. To correctly characterize cloud formation requires that we incorporate it into the chemical equilibrium computations described above; cloud formation occurs for particular elements when the phase with the minimum Gibbs free energy is the condensed phase. The only species we consider here for which this is an issue is the magnesium silicate, MgSiO_3 . Convenient expressions for the resulting condensation are given in Barshay & Lewis (1976). We are currently preparing a more comprehensive set of condensation curves for minor species using a Gibbs energy minimization routine, the results of which will be presented in a subsequent paper.

2.7. T_{eff} versus T_{10}

As in our previous papers, we parametrize the specific entropy of the fully convective deep interior of an EGP by T_{10} , which is the temperature that the interior isentrope would have if extrapolated to a pressure of 10 bars, and which may or may not equal the actual atmospheric temperature at 10 bars.

We construct a $T_{\text{eff}} - T_{10} - g$ surface by making a splined fit to the grid of non-gray model atmospheres augmented with additional $T_{\text{eff}} - T_{10} - g$ points from gray model atmospheres, as presented in Saumon *et al.* (1996). The resulting surface is shown in Figure 1. The points used to define this surface are shown as dots. Open dots represent the previous (gray-atmosphere) relations from Saumon *et al.*, and the solid dots are the new (non-gray-atmosphere) calculations. To illustrate the domain actually traversed by EGP models, three evolutionary trajectories of EGPs with masses of 1 M_J (left), 10 M_J (middle), and 42 M_J (0.04 M_\odot ; right) are shown. The earliest portions of the evolution tracks are shown as dotted lines starting at an age of 10^{-3} Gyr and ending at an age of 10^{-1} Gyr. Subsequent evolution is shown as a solid line, which ends at a maximum age of 10 Gyr for the 1 M_J and 10 M_J models, and at 20 Gyr for the 42 M_J model. Evolution of objects with ages greater than 0.1 Gyr is well constrained by our non-gray grid.

3. Atmospheres

3.1. Radiative and Convective zones

Figure 2 shows profiles of atmospheric pressure as a function of temperature calculated in our grid of non-gray models. In this figure, the surface gravity g is held constant at 2200 cm s^{-2} (close to the value for Jupiter), and T_{eff} takes the values 128 K (lowest curve), and 200 K to 1000 K (highest curve) in steps of 100 K. This sequence does not precisely

represent an evolutionary sequence for a Jupiter-mass object because g actually decreases with increasing T_{eff} in such an object. The heavy dot represents the photosphere, which is not a well-defined region in a non-gray model atmosphere, but which we approximate as the region in the atmosphere where the local temperature $T = T_{\text{eff}}$. Convection zones, where the local value of dT/dP is essentially equal to the adiabatic value, are shown as dashed lines; as usual, radiative zones appear where the local value of dT/dP is subadiabatic. Various chemical boundaries, discussed below, are shown as lighter lines, solid for a change in equilibrium for chemical species, and dashed for formation of condensed phases of a single species. The observed $P - T$ relation for Jupiter (Lindal 1992; Seiff *et al.* 1996) is shown as a dot-dashed line.

Note in Figure 2 that a detached radiative zone appears in the hotter models at temperatures around 1500 to 2000 K. The physical origin of this zone is the near-coincidence of a minimum in the CIA opacity as a function of wavelength with the maximum of the local Planck function, as originally discovered by Guillot *et al.* (1994). Guillot *et al.* have determined that a detached radiative zone is likely also to be present in Jupiter at temperatures between 1200 and 2900 K. Not only is the detached radiative zone of interest in its own right, but it is important for the evolution of EGPs because it causes the specific entropy in the uppermost convection zone to be higher than the specific entropy in the deepest convection zone. Thus, an EGP in which this zone appears will evolve slightly more rapidly than it would in the absence of the zone. That is, for a given value of T_{eff} , the central temperature will be lower than would be calculated without allowing for the detached radiative zone.

The models shown in Figure 2 do not extend to sufficient depth at $T_{\text{eff}} = 128$ K and 200 K to include the detached radiative zone. Thus, the relation between T_{eff} and T_{10} for these models is slightly incorrect. However, as discussed by Guillot *et al.* (1994) and

Ingersoll & Pollard (1982), the difference between the radiative gradient and the adiabatic gradient in the radiative zone is small, so that the cumulative error in calculating T_{10} is at the level of or smaller than other effects which we neglect in this paper, such as insolation from a moderately distant (~ 5 A.U.) companion star.

Figures 3–6 portray the calculated atmospheric profiles for surface gravities of 10^4 , 3×10^4 , 10^5 , and 3×10^5 cm s $^{-2}$. As the gravity increases, the photospheric pressure increases, but the T_{eff} dependence of the photospheric pressure is weak. For all gravities, an extended or second radiative zone is a generic feature of the atmospheres. This will have consequences for the mixing of non-equilibrium species into the observable layers.

3.2. Equilibrium and Condensation Lines

Figures 2–6 depict temperature/pressure profiles, on which are superimposed the equilibrium condensation lines for various species. For Jovian-type effective temperatures condensation of ammonia and water occur near the photosphere. Even for objects as warm as $T_{\text{eff}}=500$ K, water condensation occurs, but it does so at altitudes well above the photosphere in the atmosphere, and at pressures so low that (a) the actual cloud particle density is rather small and (b) the cloud particles are expected to fall out of the atmosphere rapidly. We therefore expect such a tenuous water cloud to play a much more minor role in the radiative balance and spectral appearance than in the cooler objects for which the water cloud is potentially quite massive (as in simplistic Jupiter models).

Interestingly, among cloud-forming species which are abundant by virtue of cosmic composition, a relatively large gap occurs between water and less volatile species. Sulfur-bearing condensates of iron sulfides (not shown in the figures) might be present in the effective temperature range around 500 K. Beyond that, magnesium silicate and iron

clouds are expected to form around the photosphere for objects with effective temperature exceeding 1000 K. All of the relationships between effective temperature and cloud formation are modestly sensitive to the effective gravity.

Also shown in Figures 2–6 are lines defining equal gas-phase abundances of methane and carbon monoxide and of ammonia and nitrogen. Le Chatelier’s principle demands that the hydrate species dominate at the lower temperatures. Hence, below ~ 1200 K and ~ 600 K, methane and ammonia, respectively, are the dominant carbon and nitrogen species. Between ~ 600 K and ~ 1200 K, N_2 and CH_4 can coexist. This illustrates that Gl229B is a threshold object which may contain some amounts of CO in addition to CH_4 . It is also possible that the atmosphere of Gl229B contains detectable amounts of ammonia, because, even though it is a minor species, it is spectroscopically active.

3.3. Clouds

Cloud formation depletes a gas-phase absorber from certain regions of the atmosphere; if this occurs around the photosphere the resulting radiative balance and emergent flux distribution are modified. Because of condensation, we expect that the gaseous water bands will disappear for objects with effective temperature below about 400 K. We expect the disappearance of silicate or iron features below about 1000 K (depending modestly on surface gravity).

Beyond predicting where the water and ammonia bands should disappear due to condensation, the spectral and radiative effects of clouds are difficult to quantify. Simple models in which clouds are uniformly distributed over the surface of the EGP, and are characterized by a single particle size, fail to take account of atmospheric dynamics which can lead to dramatic changes in the effects of clouds. In particular, convective processes

lead to growth in the mean particle size, as well as a potentially heterogeneous distribution of clouds across the disk of the object. In the case of water and magnesium silicates, the latent heat of condensation increases the mean upwelling velocity and can exaggerate these effects, as quantified by Lunine *et al.* (1989). The simple model of the transport processes in magnesium silicate clouds presented in Lunine *et al.* suggests particle sizes in the range of 100 microns are possible by coalescence, much larger than the micron-sized particles one would assume from simple condensation. The radiative properties of a cloud clearly depend upon the actual particle size, as well as the large-scale cloud morphology (broken or continuous).

The importance of these processes is seen in Jupiter. Earth-based and Voyager spectra, along with theoretical modeling, show that the spectroscopic effects of water clouds differ from those predicted by the simplest condensation models (Carlson *et al.* 1987). Galileo probe results (Niemann *et al.* 1996) demonstrate directly that global dynamical processes combined with condensation lead to a strongly heterogeneous distribution of water clouds across Jupiter’s disk. Thus, in the archtypical example of a giant planet, the simple assumptions about cloud formation and their impact on radiative processes fail. Likewise, on Neptune the methane clouds are distributed in a manifestly heterogeneous fashion.

For these reasons we have chosen not to model explicitly the spectral and radiative effects of condensed species. To do so with the available information remains an unconstrained exercise, but higher resolution spectra on objects such as G1229B could provide constraints for such cloud modeling.

4. Evolutionary Models

In Burrows *et al.* (1995) and Saumon *et al.* (1996), we published cooling curves for EGPs and small brown dwarfs that were based upon our then-current atmosphere models. For this paper, we have updated the H_2 CIA, H_2O , and CH_4 opacities and the T_{10} – T_{eff} grid. Consequently, the evolutionary tracks have changed, but generally by no more than 10% in luminosity at any given time, for any given mass. In this section, we present these latest cooling tracks and do so in the larger context of the M dwarf/brown dwarf/EGP continuum. The figures in this section cover three orders of magnitude in mass and encapsulate the characteristics of the entire family of substellar objects and the transition to stars.

Figure 7 portrays the luminosity versus time for objects from Saturn’s mass ($0.3 M_{\text{J}}$) to $0.2 M_{\odot}$. The early plateaux between 10^6 years and 10^8 years are due to deuterium burning, where the initial deuterium mass fraction was taken to be 2×10^{-5} . Deuterium burning occurs earlier, is quicker, and is at higher luminosity for the more massive models, but can take as long as 10^8 years for a $15 M_{\text{J}}$ object. The mass below which less than 50% of the “primordial” deuterium is burnt is $\sim 13 M_{\text{J}}$ (Burrows *et al.* 1995). On this and subsequent figures in this section, we have arbitrarily classed as “planets” those objects that do not burn deuterium and as “brown dwarfs” those that do burn deuterium, but not light hydrogen. While this distinction is physically motivated, we do not advocate abandoning the definition based on origin. Nevertheless, the separation into M dwarfs, “brown dwarfs”, and giant “planets” is useful for parsing by eye the information in the figures.

In Figure 7, the bumps between $10^{-4} L_{\odot}$ and $10^{-3} L_{\odot}$ and between 10^8 and 10^9 years, seen on the cooling curves of objects from $0.03 M_{\odot}$ to $0.08 M_{\odot}$, are due to silicate and iron grain formation. These effects, first pointed out by Lunine *et al.* (1989), occur for T_{eff} s between 2500 K and 1300 K. The presence of grains affects the precise mass and luminosity at the edge of the main sequence. Since grain and cloud models are problematic, there still

remains much to learn concerning their role and how to model them (§3.3 and Allard *et al.* 1997).

Figure 8 depicts the central temperature (T_c) versus central density (ρ_c) for a variety of masses between $0.3M_J$ and $0.237 M_\odot$. Superposed are isochrones from $10^{6.5}$ to $10^{9.5}$ years. For the M dwarfs, the central temperature generally rises until the object has stabilized as a star. However, near the bottom edge of the main sequence the central temperature actually decreases slightly just before stabilizing. The central density always increases with time. The highest densities are achieved by the massive brown dwarfs and hover near 1000 gm cm^{-3} for solar metallicity. They are higher for lower metallicities, reaching a peak of $\sim 2000 \text{ gm cm}^{-3}$ at zero metallicity (Burrows *et al.* 1993). The era during which T_c increases is rather brief for the “planets” and they spend most of their time cooling throughout. The “brown dwarfs” nicely straddle these two regimes.

The Figure–8 trajectories for a given mass are universal curves, independent of the metallicity and atmosphere model. They depend solely upon the equation of state and the fact that the structures are fully convective in the interior. However, the positions of the isochrones do depend upon the model specifics and vary with metallicity and boundary conditions. Note that the isochrones shear perceptibly near the “brown dwarf”–“planet” interface. Not unexpectedly, this is a consequence of the onset of deuterium burning.

For a given “brown dwarf” or EGP mass (in M_\odot), Figure 9 connects the observables T_{eff} (in K) and gravity (g , in cgs). The dashed curves are the isochrones. As is clear from the figure, gravity maps fairly directly onto mass and for no mass does g change by more than a factor of two after 10^8 years. Modeling the spectrum of a substellar object will yield estimates of T_{eff} and g . With these estimates, Figure 9 can be used to infer the mass and the age simultaneously. In fact, for a given composition and model, only two quantities are needed to derive *all* others. Bolometric luminosity and age can be used to yield mass

and radius. Effective temperature and mass can provide age and luminosity. Our fit to the UKIRT spectrum of G1229B (Marley *et al.* 1996; Geballe *et al.* 1996; Matthews *et al.* 1996; see also Oppenheimer *et al.* 1995) gave $T_{\text{eff}} \sim 900\text{--}1000$ K and $g \sim 10^{5 \pm 0.5}$ cm s⁻². Reading off of Figure 9, one obtains a mass between $20 M_J$ and $60 M_J$, with a best value near $35 M_J$, and an age between $10^{8.5}$ and $10^{9.5}$ years. The wide range in inferred G1229B parameters is a direct consequence of the weakness of our current constraints on g .

Figure 10 depicts the evolution of radius with T_{eff} , which at later times is an ersatz age. Jupiter’s current radius is near 7×10^9 centimeters. In some sense, a radius– T_{eff} plot is a compact H–R diagram, since, while luminosities for the family range nine orders of magnitude during a Hubble time, radii vary far less. Note that initially it takes longer for more massive objects to shrink, but that isochrones are not very much different from constant–radius lines at later times. Note also that the lowest mass objects (*e.g.*, Saturn) tend to have larger radii at earlier times and smaller radii at later times. In addition, at a given T_{eff} , the higher the mass the smaller the radius, while at a given age (after 10^8 years) radii generally decrease with mass. Not obvious from the plot is the fact that the maximum cold radius occurs for a mass near $4 M_J$.

Figure 11 is a theorist’s H–R diagram for the “brown dwarfs” and giant “planets.” The inset is a continuation of the figure down to low luminosities and T_{eff} s. The current Jupiter and Saturn are superposed for comparison (Pearl & Conrath 1991). Importantly, constant mass trajectories never cross and it is only for objects below $25 M_J$ that temperatures below 400 K are reached within 10^{10} years. Figures 7 through 11 collectively summarize the model space within which substellar objects reside. Tables 1a-1d contain the results of evolutionary calculations for objects with masses of $1 M_J$, $5 M_J$, $10 M_J$, and $0.04 M_\odot$ ($\sim 42 M_J$). The numbers in them represent the latest atmospheric and opacity calculations at solar metallicity.

5. EGP and Brown Dwarf Spectra

There are a few major aspects of EGP/brown dwarf atmospheres that bear listing and that uniquely characterize them. Below T_{eff} s of 1300 K, the dominant equilibrium carbon molecule is CH_4 , not CO, and below 600 K the dominant nitrogen molecule is NH_3 , not N_2 . As discussed in §2, the major opacity sources are H_2 , H_2O , CH_4 , and NH_3 . For T_{eff} s below ~ 400 K, water clouds form at or above the photosphere and for T_{eff} s below 200 K, ammonia clouds form (*viz.*, Jupiter). Collision-induced absorption of H_2 partially suppresses emissions longward of $\sim 10 \mu\text{m}$. The holes in the opacity spectrum of H_2O that define the classic telluric IR bands also regulate much of the emission from EGP/brown dwarfs in the near infrared. Importantly, the windows in H_2O and the suppression by H_2 conspire to force flux to the blue for a given T_{eff} . The upshot is an exotic spectrum enhanced relative to the blackbody value in the J and H bands ($\sim 1.2 \mu\text{m}$ and $\sim 1.6 \mu\text{m}$, respectively) by as much as *two to ten* orders of magnitude, depending upon T_{eff} . In addition, as T_{eff} decreases below ~ 1000 K, the flux in the M band ($\sim 5 \mu\text{m}$) is progressively enhanced relative to the blackbody value. While at 1000 K there is no enhancement, at 200 K it is near 10^5 . Hence, the J , H , and M bands are the premier bands in which to search for cold substellar objects. The Z band ($\sim 1.05 \mu\text{m}$) is also super-blackbody over this T_{eff} range. However, there is a NH_3 feature in the Z band that is not in our database. This will likely reduce the flux in this band for the cooler models. Eventhough K band ($\sim 2.2 \mu\text{m}$) fluxes are generally higher than blackbody values, H_2 and CH_4 absorption features in the K band decrease its importance *relative* to J and H . As a consequence of the increase of atmospheric pressure with decreasing T_{eff} , the anomalously blue $J - K$ and $H - K$ colors get *bluer*, not redder.

For this paper, we calculated low-resolution spectra from $0.9 \mu\text{m}$ to $2500 \mu\text{m}$, though we focus our discussions on the $1 \mu\text{m}$ to $10 \mu\text{m}$ region. A grid of spectra in T_{eff} –gravity

space was calculated. As stated in §2.7, for the evolutionary calculations described in §4, a $T_{\text{eff}}-T_{10}$ grid was also constructed. The evolutionary calculations were used to map mass and age onto T_{eff} and gravity, which were then used to interpolate in the grid of spectra to find the spectra and colors at any mass and age. This procedure proved to be quite robust for T_{eff} s between 1250 K and 100 K. The spectra we present are for objects in isolation and ignore the transport effect of clouds. As stated in §3.3, omitting the direct effects of clouds has consequences, for below 400 K the formation of H_2O clouds partially depletes the spectrum of the H_2O vapor features that define it at higher temperatures. Note that the presence or absence of clouds strongly affects the reflection albedos of EGPs and brown dwarfs. In particular, when there are clouds at or above the photosphere, the albedo in the optical is high. Conversely, when clouds are absent, the albedo in the mostly absorbing atmosphere is low.

Figure 12 depicts the object’s surface flux versus wavelength for representative T_{eff} s from 130 K to 1000 K at a gravity of $3.0 \times 10^4 \text{ cm s}^{-2}$. The corresponding masses range from $\sim 13 M_J$ to $\sim 16 M_J$ and the corresponding ages range from 0.25 Gyrs to 7 Gyrs. Superposed on Figure 12 are the positions of various prominent molecular bands and the J , H , K , and M bands. As is clear from the figure, H_2O defines much of the spectrum, but CH_4 and H_2 modify it in useful ways. CH_4 absorption features near $1.65 \mu\text{m}$, $2.2 \mu\text{m}$, and $3.3 \mu\text{m}$ are particularly relevant, the latter two decreasing the K and L' ($\sim 3.5 \mu\text{m}$) band fluxes, respectively. NH_3 near $6 \mu\text{m}$ becomes important below 250 K and the CH_4 feature around $7.8 \mu\text{m}$ deepens with decreasing T_{eff} . However, it should be noted that in Jupiter the $7.8 \mu\text{m}$ absorption feature is inverted into a stratospheric emission feature. Since a stratosphere requires UV flux from the primary or another energy deposition mechanism, our models do not address this possibility. In addition, we find that H_2O and NH_3 features near $6 \mu\text{m}$ make the band from 5.5 to $7 \mu\text{m}$ less useful for searching for brown dwarfs and EGPs.

Figure 13 depicts spectra between $1\ \mu\text{m}$ and $40\ \mu\text{m}$ at a detector 10 parsecs away from objects with age 1 Gyr and masses from $1\ M_J$ through $40\ M_J$. Figure 14 portrays the spectra for the same parameters, but from $1\ \mu\text{m}$ to $10\ \mu\text{m}$. Superposed on the former are the corresponding blackbody curves and superposed on both are putative sensitivities for the three NICMOS cameras (Thompson 1992), ISO (Benvenuti *et al.* 1994), SIRTf (Erickson & Werner 1992), and Gemini/SOFIA (Mountain *et al.* 1992; Erickson 1992). Figure 13 demonstrates how unlike a blackbody an EGP spectrum is. Note on Figure 13 the H_2 -induced suppression at long wavelengths and the enhancement at shorter wavelengths. For example, the enhancement at $5\ \mu\text{m}$ for a 1 Gyr old, $1\ M_J$ extrasolar planet is by four orders of magnitude. Implicit in Figure 13 is the enhancement around the N band ($\sim 10\ \mu\text{m}$) for T_{eff} below 200 K.

Comparison with the sensitivities reveals that the range for detection by SIRTf at $5\ \mu\text{m}$ of a 1 Gyr old, $1\ M_J$ object in isolation is near 100 parsecs. The range for NICMOS in H for a 1 Gyr old, $5\ M_J$ object is approximately 300 parsecs, while for a coeval $40\ M_J$ object it is near 1000 parsecs. These are dramatic numbers that serve to illustrate both the promise of the new detectors and the enhancements we theoretically predict.

Figures 15–19 portray the evolution from 0.1 Gyr to 5 Gyr of the spectra from $1\ \mu\text{m}$ to $10\ \mu\text{m}$ of objects with masses of 1, 5, 10, 15, $20\ M_J$. The higher curves are for the younger ages. These cooling curves summarize EGP/brown dwarf spectra and their evolution, but are merely representative of the suite of models now available. Note that the scales change from Figures 15–16 to Figures 17–19 and that, for comparison, blackbody curves are superposed on Figure 15 (the “Jupiter” model). Figures 17 and 19 include identifications of some of the molecular features. Figure 19 suggests that SIRTf will be able to see at $5\ \mu\text{m}$ a 5 Gyr old, $20\ M_J$ object in isolation out to ~ 400 parsecs and that NICMOS will be able to see at J or H a 0.1 Gyr old object with the same mass out to ~ 2000 parsecs. As shown in

Figure 15, the J and H flux enhancements over blackbody values for the $1 M_J$ model after 0.1 Gyr are at least ten orders of magnitude. However, it must be remembered that these models do not include a reflected light component from a primary. For many combinations of primary and orbital separation, this reflected component can dominate in the near IR.

6. Infrared Colors

From the spectra described in the previous section, we have calculated infrared colors and produced color–color and color–magnitude diagrams. Figures 20 through 24 are representative color–magnitude diagrams for objects with masses from $3 M_J$ to $40 M_J$, for ages of 0.5, 1.0, and 5.0 Gyr. Figures 25 and 26 are color–color diagrams for the same models. For comparison, included in these figures are the corresponding blackbody curves, hot, young brown dwarf or extremely late M dwarf candidates such as LHS2924, GD 165B, Calar 3, and Teide 1 (Kirkpatrick, Henry, & Simons 1994,1995; Zapatero-Osorio, Rebolo, & Martin 1997), and a sample of M dwarfs from Leggett (1992). These figures collectively illustrate the unique color realms occupied by extrasolar giant planets and brown dwarfs.

Figures 20 and 21 portray the fact that the K and J versus $J - K$ infrared H–R diagrams loop back to the blue below the edge of the main sequence and are not continuations of the M dwarf sequence into the red. The difference between the blackbody curves and the model curves is between 3 and 10 magnitudes for J versus $J - K$, more for K versus $J - K$. Gl229B fits nicely on these theoretical isochrones. The suppression of K by H_2 and CH_4 features is largely responsible for this anomalous blueward trend with decreasing mass and T_{eff} . As Figures 22 and 23 demonstrate, the fit to Gl229B in H is not as good. This is also true of the fit to L' . Since both H and L' have significant CH_4 features in them, we surmise that incompleteness or errors in the CH_4 opacity database is the culprit. As Figures 22 and 23 also show, $J - H$ actually reddens with decreasing T_{eff} ,

but only marginally and is still 1.5 to 4 magnitudes bluer than the corresponding blackbody. That the $J - H$ and $H - K$ colors of EGPs and brown dwarfs are many magnitudes blueward of blackbodies is a firm conclusion of this work.

Superposed on the color-color diagrams (Figures 25 and 26) are model colors for stars at the edge of the main sequence for metallicities from solar to 10^{-3} times solar. For the non-solar calculations, the atmospheres of Allard & Hauschildt (1995) were used to generate the corresponding $T_{\text{eff}}-T_{10}$ relations employed by our evolutionary code (Saumon *et al.*, in preparation). A glance at these numbers and those in the zero-metallicity paper of Saumon *et al.* (1994) reveals that we expect the lower metallicity models to populate the bluer regions below the depicted model lines. However, we have yet to calculate precise numbers for non-solar metallicities with the new algorithms and opacities of this paper.

Tables 2 and 3 depict the infrared magnitudes and colors for various gravities and T_{eff} s. Also included are N band magnitudes and $M - N$ colors. We employed the transmission curves of Bessell & Brett (1988) and Bessell (1990) to define the photometric bandpasses and the model of Vega by Dreiling & Bell (1980) for the calibration of the magnitude scale. As Table 2 and Figures 20–24 suggest, the brightnesses in the near IR are quite respectable. Table 3 shows that colors generally get bluer with increasing gravity (except for $K - L'$, which shows the opposite trend). For $J - H$, the effect may be only ~ 0.2 magnitudes per decade in gravity and for the problematic $H - K$ color it is perhaps ~ 0.4 magnitudes per decade. However, for $K - L'$ it is ~ 0.8 magnitudes per decade, though one must recall that L' is not well modeled. Nevertheless, in principle these colors can collectively be used as crude gravity diagnostics.

7. Conclusions and Future Work

During the past two years, scientists and the public at large have been galvanized by the discovery of planets and brown dwarfs around nearby stars and by evidence for ancient life on Mars (McKay *et al.* 1996). These extraordinary findings have dramatically heightened interest in the age-old questions of where we came from and whether we are unique in the cosmos. NASA has outlined a program to detect planetary systems around nearby stars that may become a future focus of NASA and its central, unifying scientific theme in the next century. This vision is laid out in the *Exploration of Neighboring Planetary Systems (ExNPS) Roadmap* (see also the “TOPS” Report, 1992) and has been expanded to include the Origins of life, planets, galaxies, and the universe.

The next generation planet and brown dwarf searches and studies will be conducted by NICMOS, SIRTf, Gemini/SOFIA, ISO, NGST, LBT (Angel 1994), the MMT conversion, the VLT, Keck I & II, COROT (transits), DENIS, 2MASS, UKIRT, and IRTF, among other platforms. For close companions, advances in adaptive optics, interferometry, and coronagraphs will be necessary to disentangle the light of companion and primary.

The models we have generated of the colors and spectra of EGPs and brown dwarfs are in aid of this quest for Origins and of the discovery and characterization of substellar objects around nearby stars and in the field. We have created a general non-gray theory of objects from $0.3 M_J$ to $70 M_J$ below ~ 1300 K using the best input physics and some of the best numerical tools available, but much remains to be done. In particular, the opacity of CH_4 and a proper treatment of silicate/iron, H_2O , and NH_3 clouds are future challenges that must be met before the theory can be considered mature. Furthermore, the effects of stellar insolation, addressed only approximately in Saumon *et al.* (1996) and Guillot *et al.* (1996), must be incorporated consistently. Since the near IR signature of proximate substellar companions will be significantly altered by a reflected component, a theory of

albedos in the optical and in the near IR must be developed. For specificity, we focussed in this paper upon objects in isolation and did not include the complicating parameters of central star and semi-major axis. However, it will be useful to predict the signatures of specific systems with known orbital characteristics, primaries, and ages, such as τ Boo, 51 Peg, v And, 55 Cnc, ρ CrB, 70 Vir, 16 Cyg, and 47 UMa.

Nevertheless, our theoretical calculations lead to certain general conclusions:

1. H_2O , H_2 , and CH_4 dominate the spectrum below $T_{\text{eff}} \sim 1200$ K. For such T_{eff} s, most or all true metals are sequestered below the photosphere.
2. Though EGP colors and low-resolution spectra depend upon gravity, this dependence is weak. However, high-resolution spectra may provide useful gravity diagnostics.
3. The primary bands in which to search are Z , J , H , K , M and N . K is not as good as J or H .
4. Enhancements and suppressions of the emergent flux relative to blackbody values can be by many orders of magnitude.
5. Objects that were considered from their low T_{eff} s ($\lesssim 600$ K) to be undetectable in the near IR may not be.
6. The infrared colors of EGPs and brown dwarfs are much bluer than the colors previously derived using either the blackbody assumption or primitive non-gray models.
7. In some IR colors (*e.g.*, $J - K$), an object gets bluer, not redder, with age and for a given age, lower-mass substellar objects are bluer than higher-mass substellar objects.

8. For a given composition, only two observables are necessary to constrain a substellar object's parameters. For instance, given only T_{eff} and gravity, one can derive mass, age, and radius.
9. The existence of an interior radiative zone seems to be a generic feature of substellar objects with T_{eff} s from ~ 200 K to 1000 K, and might also obtain for T_{eff} s below ~ 200 K. The appearance and extent of such a radiative zone is a function of gravity.
10. Clouds of H_2O and NH_3 are formed for T_{eff} s below ~ 400 K and ~ 200 K, respectively. Their formation will affect the colors and spectra of EGPs and brown dwarfs in ways not yet fully characterized.

We thank R. Angel, W. Benz, S. Kulkarni, J. Liebert, B. Oppenheimer, G. Rieke, G. Schneider, S. Stolovy, and N. Woolf for a variety of useful contributions. This work was supported under NSF grants AST-9318970 and AST-9624878 and under NASA grants NAG5-2817, NAGW-2250, and NAG2-6007.

REFERENCES

- Allard, F., & Hauschildt, P.H. 1995, ApJ, 445, 433
- Allard, F., Hauschildt, P.H., Baraffe, I., & Chabrier, G. 1996, ApJ, 465, L123
- Allard, F., Hauschildt, P. H., Alexander, D. R. & Starrfield, S. 1997, ARA&A, 35, 137
- Anders, E. & Grevesse, N. 1989, Geochim. Cosmochim. Acta, 53, 197
- Angel, J.R.P. 1994, Nature, 368, 203
- Barshay, S.S. & Lewis, J.S. 1976, ARA&A, 14, 81
- Benvenuti, P. *et al.* 1994, in *ESA's Report to the 30th COSPAR Meeting, ESA SP-1169, Paris*, p. 75 (ISO)
- Borysow, A. & Frommhold, L. 1990, ApJ, 348, L41
- Brown, L.R. & Peterson, D.B. 1994, J. Mol. Spect., 168, 593
- Brown, L.R. & Plymate, C. 1996, J. Quant. Spect. Rad. Transfer, 56, 263
- Bulanin, M.O., Dokuchaev, A.B., Tonkov, M.V., & Filippov, N.N. 1984, J. Quant. Spect. Rad. Transfer, 6, 521
- Burrows, A., Hubbard, W.B., & Lunine, J.I. 1989, ApJ, 345, 939
- Burrows, A., Hubbard, W.B., Saumon, D., & Lunine, J.I. 1993, ApJ, 406, 158
- Burrows, A., Saumon, D., Guillot, T., Hubbard, W.B., & Lunine, J.I. 1995, Nature, 375, 299
- Bessell, M.S. 1990, PASP, 102, 1181
- Bessell, M.S., & Brett, J.M. 1988, PASP, 100, 1134
- Butler, R. P. & Marcy, G. W. 1996, ApJ, 464, L153
- Butler, R. P., Marcy, G. W., Williams, E., Hauser, H., & Shirts, P. 1997, ApJ, 474, L115

- Carbon, D.F. & Goorvitch, D. 1996, *Bull. Am. Astr. Society*, 189, 81.03
- Carlson, B.E., Prather, M.J., & Rossow, W.B. 1987, *ApJ*, 322, 559
- Cochran, W.D., Hatzes, A.P., Butler, R.P., & Marcy, G. 1997, *Science*, in press
- D’Antona, F. & Mazzitelli, I. 1985, *ApJ*, 296, 502
- Dorman, B., Nelson, L.A., & Chou, W.Y. 1989, *ApJ*, 342, 1003
- Dreiling, L.A. & Bell, R.A. 1980, *ApJ*, 241, 736
- Eisenberg, D. & Kauzmann, W. 1969, *The Structure and Properties of Water* (New York: Oxford University Press)
- Erickson, E. F. 1992, *Space Science Reviews*, 61, 61 (SOFIA)
- Erickson, E. F. & Werner, M. W. 1992, *Space Science Reviews*, 61, 95 (SIRTF)
- ExNPS: A Road Map for the Exploration of Neighboring Planetary Systems, JPL Publication 96–22, August 1996
- Fegley, B. & Lodders, K. 1994, *Icarus*, 110, 117
- Fegley, B. & Lodders, K. 1996, *ApJ*, 472, L37
- Gamache, R.R., Lynch, R., & Brown, L.R. 1996, *J. Quant. Spect. Rad. Transfer*, 56, 471
- Geballe, T. R., Kulkarni, S. R., Woodward, C. E., & Sloan, G. C. 1996, *ApJ*, 467, L101
- Goody, R., West, R., Chen, L., & Crisp, D. 1989, *J. Quant. Spectr. Rad. Transfer*, 42, 539
- Goorvitch, D. 1994, *ApJS*, 95, 535
- Grossman, A.S. & Grant, K. 1992, LLNL Rept. UCRL-ID-111805
- Grossman, A.S. & Grant, K. 1994a, LLNL Rept. UCRL-ID-116533
- Grossman, A.S. & Grant, K. 1994b Eighth Conference on Atmospheric Radiation, 97, American Meteorological Society.

- Guillot, T., Burrows, A., Hubbard, W.B., Lunine, J.I., & Saumon, D. 1996, ApJ, 459, L35
- Guillot, T., Gautier, D., Chabrier, G., & Mosser, B. 1994, Icarus, 112, 337
- Handbook of Chemistry and Physics, 74th Edition, 1993, ed. D.R. Lide, CRC Press Inc.
- Husson, N., Bonnet, B., Scott, N.A., & Chedin, A. 1994, J. Quant. Spect. Rad. Transfer, 48, 509
- Ingersoll, A.P. & Pollard, D. 1982, Icarus 52, 62
- ISO Observer’s Manual Version 2.0, 31 March 1994, prepared by the ISO Science Operations Team, p6
- Kirkpatrick, J.D., Henry, T.J., & Simons, D.A. 1994, AJ, 108, 1437
- Kirkpatrick, J.D., Henry, T.J., & Simons, D.A. 1995, AJ, 109, 797
- Kurucz, R.L., 1970, Smithsonian Obs. Spec. Rep., 309, 1-291
- Lacis, A.A. & Oinas, V. 1991, J. Geophys. Res., 96, 9027
- Lange’s Handbook of Chemistry, 1979, ed. J.A. Dean, McGraw-Hill Book Company, New-York
- Latham, D. W., Mazeh, T., Stefanik, R.P., Mayor, M., & Burki G. 1989, Nature, 339, 38
- Leger, A., *et al.* 1993, Darwin Mission Concept, proposal to ESA
- Leggett, S.K. 1992, ApJS, 82, 351
- LeMoal, M.F. & Severin, F. 1986, J. Quant. Spect. Rad. Transfer, 35, 145
- Levy, A., Lacome, N., & Tarrago, G. 1994, J. Mol. Spect., 166, 20
- Lindal, G. 1992, AJ, 103, 967
- Lunine, J.I., Hubbard, W.B., Burrows, A., Wang, Y.P., & Garlow, K. 1989, ApJ, 338, 314
- Marcy, G. W. & Butler, R. P. 1996, ApJ, 464, L147

- Margolis, J. 1993, *J. Quant. Spect. Rad. Transfer*, 50, 431
- Margolis, J. 1996, *J. Quant. Spect. Rad. Transfer*, 55, 823
- Marley, M., Saumon, D., Guillot, T., Freedman, R.S., Hubbard, W.B., Burrows, A., & Lunine, J.I. 1996, *Science*, 272, 1919
- Matthews, K., Nakajima, T., Kulkarni, S.R., & Oppenheimer, B.R. 1996, *AJ*, 112, 1678
- Mayor, M. & Queloz, D. 1995, *Nature*, 378, 355
- McKay, D. S., *et al.* 1996, *Science*, 273, 924
- McKay, C.P, Pollack, J.B., & Courtin, R. 1989, *Icarus*, 80, 23
- Moses, J.I., Allen, M., & Yung, Y.L. 1992, *Icarus*, 99, 318
- Mountain, M., R. Kurz, R., & Oschmann, J. 1994, in *The Gemini 8-m Telescope Projects, S.P.I.E. Proceedings on Advanced Technology Optical Telescopes V*, 2199, p. 41 (Gemini)
- Nakajima, T., Oppenheimer, B.R., Kulkarni, S.R., Golimowski, D.A., Matthews, K., & Durrance, S.T. 1995, *Nature*, 378, 463
- Nelson, L.A., Rappaport, S.A., & Joss, P.C. 1985, *Nature* 316, 42
- Niemann, H., Atreya, S.K., Cargnan, G.R., Donahue, T.M., Haberman, J.A., Harpold, D.N., Hartle, R.E., Hunten, D.M., Kasprzak, W.T., Mahaffy, P.R., Owen, T.C., Spencer, N.W., Way, S.H. 1996, *Science*, 272, 837
- Oppenheimer, B.R., Kulkarni, S.R., Matthews, K., & Nakajima, T. 1995, *Science*, 270, 1478
- Partridge, H. & Schwenke, D.W. 1997, *J. Chem. Phys.*, 106, 4618
- Pearl, J. C. & Conrath, R. A. 1991, *J. Geophys. Res. Suppl.*, 96, 18921
- Podolak, M., Hubbard, W.B. & Pollack, J.B. 1993, in *Protostars and Planets III*, eds. E.H. Levy and J.I. Lunine (Tucson, Univ. of Arizona Press), 1109.

- Polyansky, O.L., Jensen, P., & Tennyson, J. 1994, J. Phys. Chem., 101, 7651
- Rages, K., Pollack, J.B., Tomasko, M.G., & Doose, L.R. 1991, Icarus, 89, 359
- Riviere, Ph., Soufiani, A., & Taine, J. 1992, J. Quant. Spect. Rad. Transfer, 48, 187
- Riviere, Ph., Soufiani, A., & Taine, J. 1994, J. Quant. Spect. Rad. Transfer, 53, 335
- Rothman, L.S., Gamache, R.R., Tipping, R.H., Rinsland, C.P., Smith, M.A.H., Benner, D.C., Malathy Devi, V., Flaud, J.-M., Camy-Peyret, C., Perrin, A., Goldman, A., Massie, S.T., Brown, L.R., & Toth, R.A. 1992, J. Quant. Spect. Rad. Transfer, 48, 469.
- Rothman, L.S., Wattson, R.B., Gamache, R.R., Goorvitch, D., Hawkins, R.L., Selby, J.E.A., Cambry-Peyret, C., Flaud, J.-M., Schroeder, J., & McCann, A. 1997, J. Quant. Spect. Rad. Transfer, submitted
- Saumon, D., Bergeron, P., Lunine, J.I., Hubbard, W.B. & Burrows, A. 1994, ApJ, 424, 333
- Saumon, D., Hubbard, W.B., Burrows, A., Guillot, T., Lunine, J.I., & Chabrier, G. 1996, ApJ, 460, 993
- Saumon, D. & Chabrier, G. 1991, Phys. Rev. A, 44, 5122
- Saumon, D. & Chabrier, G. 1992, Phys. Rev. A, 46, 2084
- Saxner, M. & Gustafsson, B. 1984, Astron. Astrophys. , 140, 334
- Seiff, A., *et al.* 1996, Science, 272, 844
- Stevenson, D. J. 1991, ARA&A, 29, 163
- Stringfellow, G. S. 1991, ApJ, 375, L21
- Thompson, R. 1992, Space Science Reviews, 61, 69 (NICMOS)
- Tipping, R. 1990, Report on Calculation of Spectroscopic Parameters for Diatomic Molecules of Atmospheric Interest, Univ. of Alabama Report, Dept. of Physics and Astronomy

- Toon, O.B., McKay, C.P., Ackerman, T.P., & Santhanam, K. 1989, *J. Geophys. Res.*, 94, 16287
- TOPS: Toward Other Planetary Systems, NASA Solar System Exploration Division, Washington, D.C., 1992
- Tsuji, T., Ohnaka, W., Aoki, W., & Nakajima, T. 1996, *Astron. Astrophys.* , 308, L29
- Tyuterev, V.I.G., Babikov, Yu.L., Tashkun, S.A., Perevalov, V.I., Nikitin, A., Champion, J.-P., Wegner, Ch., Pierre, C., Pierre, G., Hilico, J.-C., & Loete, M. 1994, *J. Quant. Spect. Rad. Transfer*, 52, 459
- Wattson, R.B., and Rothman L.S. 1992, *J. Quant. Spectr. Rad. Transfer*, 48, 763
- Zapatero-Osorio, M.R., Rebolo, R., & Martin, E.L. 1997, *Astron. Astrophys.* , 317, 164
- Zheng, C. & Borysow, A. 1995, *Icarus*, 113, 84

Fig. 1.— $T_{\text{eff}}-T_{10}-g$ surface used for evolutionary calculations presented in this paper.

Fig. 2.— Atmospheric pressure–temperature profiles for EGPs with surface gravity fixed at 2200 cm s^{-2} and $T_{\text{eff}} = 1000, 900, 800, 700, 600, 500, 400, 300, 200$, and 128 K .

Fig. 3.— Atmospheric pressure–temperature profiles for EGPs with surface gravity fixed at 10^4 cm s^{-2} and $T_{\text{eff}} = 800, 600, 500, 400, 200$, and 128 K .

Fig. 4.— Atmospheric pressure–temperature profiles for EGPs with surface gravity fixed at $3 \times 10^4 \text{ cm s}^{-2}$ and $T_{\text{eff}} = 1100, 900, 700, 300, 200$, and 128 K .

Fig. 5.— Atmospheric pressure–temperature profiles for EGPs with surface gravity fixed at 10^5 cm s^{-2} and $T_{\text{eff}} = 1200, 1100, 900, 700, 500, 250, 200$, and 128 K .

Fig. 6.— Atmospheric pressure–temperature profiles for EGPs with surface gravity fixed at $3 \times 10^5 \text{ cm s}^{-2}$ and $T_{\text{eff}} = 1200, 1100, 900, 700, 200$, and 128 K .

Fig. 7.— Evolution of the luminosity (in L_{\odot}) of solar–metallicity M dwarfs and substellar objects versus time (in years) after formation. The stars, “brown dwarfs” and “planets” are shown as solid, dashed, and dot–dashed curves, respectively. In this figure, we arbitrarily designate as “brown dwarfs” those objects that burn deuterium, while we designate those that do not as “planets.” The masses in M_{\odot} label most of the curves, with the lowest three corresponding to the mass of Saturn, half the mass of Jupiter, and the mass of Jupiter.

Fig. 8.— Evolutionary tracks of central density (in gm cm^{-3}) versus central temperature (in K) for stars (solid), “brown dwarfs” (dashed) and “giant planets”(dot–dashed), as in Figure 7. The isochrones are drawn as gray curves and are labeled in \log_{10} years. The pronounced wave in the isochrones between about $\log_{10} T_c = 5.5$ and 6 is due to deuterium burning. A given mass defines a unique relationship between central temperature and density which is independent of metallicity. The only effect of the metallicity is to change the rate at which

the central temperature and density evolve and the positions of the isochrones.

Fig. 9.— Evolutionary tracks of \log_{10} gravity (in cm s^{-2}) versus effective temperature (in K) for “brown dwarfs” (solid) and “planets” (dashed). The isochrones are gray curves and are labeled in \log_{10} years. In all cases, gravity increases with time. Initially for the more massive brown dwarfs, the effective temperature is roughly constant, or slightly increasing, before decreasing inexorably at later times. This figure depicts how T_{eff} and gravity map onto mass and age.

Fig. 10.— \log_{10} radius (in centimeters) versus effective temperature (T_{eff} , in K), with T_{eff} decreasing to the right. This plot has the advantage over an H-R diagram that considerably more detail can be shown over the range of conditions considered. In all cases, radius decreases with time. As depicted in Figure 9, for the more massive brown dwarfs the effective temperature initially increases before decreasing.

Fig. 11.— H-R diagram: luminosity (in L_{\odot}) versus T_{eff} (in K) for various masses labeled on the figure in M_{\odot} . Due to the large range in luminosity and the near degeneracy of the tracks of substellar objects at late stages of evolution, it is not possible to represent with adequate detail the whole H-R diagram as one figure. Accordingly, the low-temperature and low-luminosity tail of the H-R diagram is shown in the inset; note that the axes are scaled differently, but otherwise correspond to those on the main figure. For additional clarity, several masses have been omitted in the inset. We have labeled the observed positions of Jupiter and Saturn as points “J” and “S,” respectively (Pearl & Conrath 1991). As discussed in Figure 7, all substellar objects decrease in luminosity monotonically, though during the early phases deuterium burning slows the evolution. As the “brown dwarfs” and “planets” cool to their cold radii, their tracks in the lower right of the H-R diagram correspond closely to curves of constant radius. Moreover, in the late phases of evolution, due to the very weak dependence of radius on mass, the curves of the lower-mass objects become degenerate.

Fig. 12.— Surface flux (in $\text{erg cm}^{-2} \text{sec}^{-1} \text{Hz}^{-1}$) versus wavelength (in microns) from $1 \mu\text{m}$ to $10 \mu\text{m}$ for T_{eff} s of 130, 200, 300, 500, 600, 700, and 1000 K, at a surface gravity of $3.0 \times 10^4 \text{ cm s}^{-2}$. Shown are the positions of the J , H , K , and M bands and various molecular absorption features. See the text for discussion.

Fig. 13.— The flux (in $\mu\text{Janskys}$) at 10 parsecs versus wavelength (in microns) from $1 \mu\text{m}$ to $40 \mu\text{m}$ for 1, 5, 10, 20, 30, and $40M_J$ models at 1 Gyr. Superposed for comparison are the corresponding blackbody curves (dashed) and the putative sensitivities of the three NICMOS cameras, ISO, Gemini/SOFIA, and SIRTf. NICMOS is denote with large black dots, ISO with thin, dark lines, Gemini/SOFIA with thin, light lines, and SIRTf with thicker, dark lines. At all wavelengths, SIRTf’s projected sensitivity is greater than ISO’s. SOFIA’s sensitivity overlaps with that of ISO around $10\mu\text{m}$. For other wavelength intervals, the order of sensitivity is $\text{SIRTf} > \text{Gemini/SOFIA} > \text{ISO}$, where $>$ means “is more sensitive than.” Note the suppression relative to the blackbody values at the longer wavelengths.

Fig. 14.— The flux at 10 parsecs (in $\mu\text{Janskys}$) versus wavelength (in microns) for the same models depicted in Figure 13, but for a wavelength range of $1 \mu\text{m}$ to $10 \mu\text{m}$. Shown are the positions of the J , H , K , and M bands and various molecular absorption features. Also included are the estimated sensitivities of NICMOS, ISO, Gemini/SOFIA, and SIRTf, as described in the caption to Figure 13.

Fig. 15.— The flux (in $\mu\text{Janskys}$) at 10 parsecs versus wavelength (in microns) from $1 \mu\text{m}$ to $10 \mu\text{m}$ for a $1M_J$ object at ages of 0.1, 0.5, 1.0, and 5.0 Gyr. Superposed are the positions of the J , H , K , and M bands and the corresponding blackbody curves (dashed), as well as the estimated sensitivities of the three NICMOS cameras, ISO, Gemini/SOFIA, and SIRTf (see caption to Figure 13).

Fig. 16.— The flux (in $\mu\text{Janskys}$) at 10 parsecs versus wavelength (in microns) from $1 \mu\text{m}$

to $10\ \mu\text{m}$ for a $5\ M_{\text{J}}$ object at ages of 0.1, 0.5, 1.0, and 5.0 Gyr. Superposed are the positions of the J , H , K , and M bands and the estimated sensitivities of the three NICMOS cameras, ISO, Gemini/SOFIA, and SIRTf.

Fig. 17.— The flux (in $\mu\text{Janskys}$) at 10 parsecs versus wavelength (in microns) from $1\ \mu\text{m}$ to $10\ \mu\text{m}$ for a $10\ M_{\text{J}}$ object at ages of 0.1, 0.5, 1.0, and 5.0 Gyr. Superposed are the positions of the J , H , K , and M bands, the estimated sensitivities of the three NICMOS cameras, ISO, Gemini/SOFIA, and SIRTf, and the positions of various of the important molecular absorption features.

Fig. 18.— The flux (in $\mu\text{Janskys}$) at 10 parsecs versus wavelength (in microns) from $1\ \mu\text{m}$ to $10\ \mu\text{m}$ for a $15\ M_{\text{J}}$ object at ages of 0.1, 0.5, 1.0, and 5.0 Gyr. Superposed are the positions of the J , H , K , and M bands and the estimated sensitivities of the three NICMOS cameras, ISO, Gemini/SOFIA, and SIRTf.

Fig. 19.— The flux (in $\mu\text{Janskys}$) at 10 parsecs versus wavelength (in microns) from $1\ \mu\text{m}$ to $10\ \mu\text{m}$ for a $20\ M_{\text{J}}$ object at ages of 0.1, 0.5, 1.0, and 5.0 Gyr. Superposed are the positions of the J , H , K , and M bands, the estimated sensitivities of the three NICMOS cameras, ISO, Gemini/SOFIA, and SIRTf, and the positions of various of the important molecular absorption features.

Fig. 20.— Absolute J vs. $J-K$ color-magnitude diagram. Theoretical isochrones are shown for $t = 0.5, 1$, and 5 Gyr, along with their blackbody counterparts. The difference between blackbody colors and model colors is striking. The brown dwarf, Gliese 229B (Oppenheimer *et al.* 1995), the young brown dwarf candidates Calar 3 and Teide 1 (Zapatero-Osorio, Rebolo, & Martin 1997), and late M dwarfs LHS 2924 and GD165B (Kirkpatrick, Henry, & Simons 1994,1995)) are plotted for comparison. The lower main sequence is defined by a selection of M-dwarf stars from Leggett (1992).

Fig. 21.— Absolute K vs. $J - K$ color–magnitude diagram. Otherwise as in Figure 20.

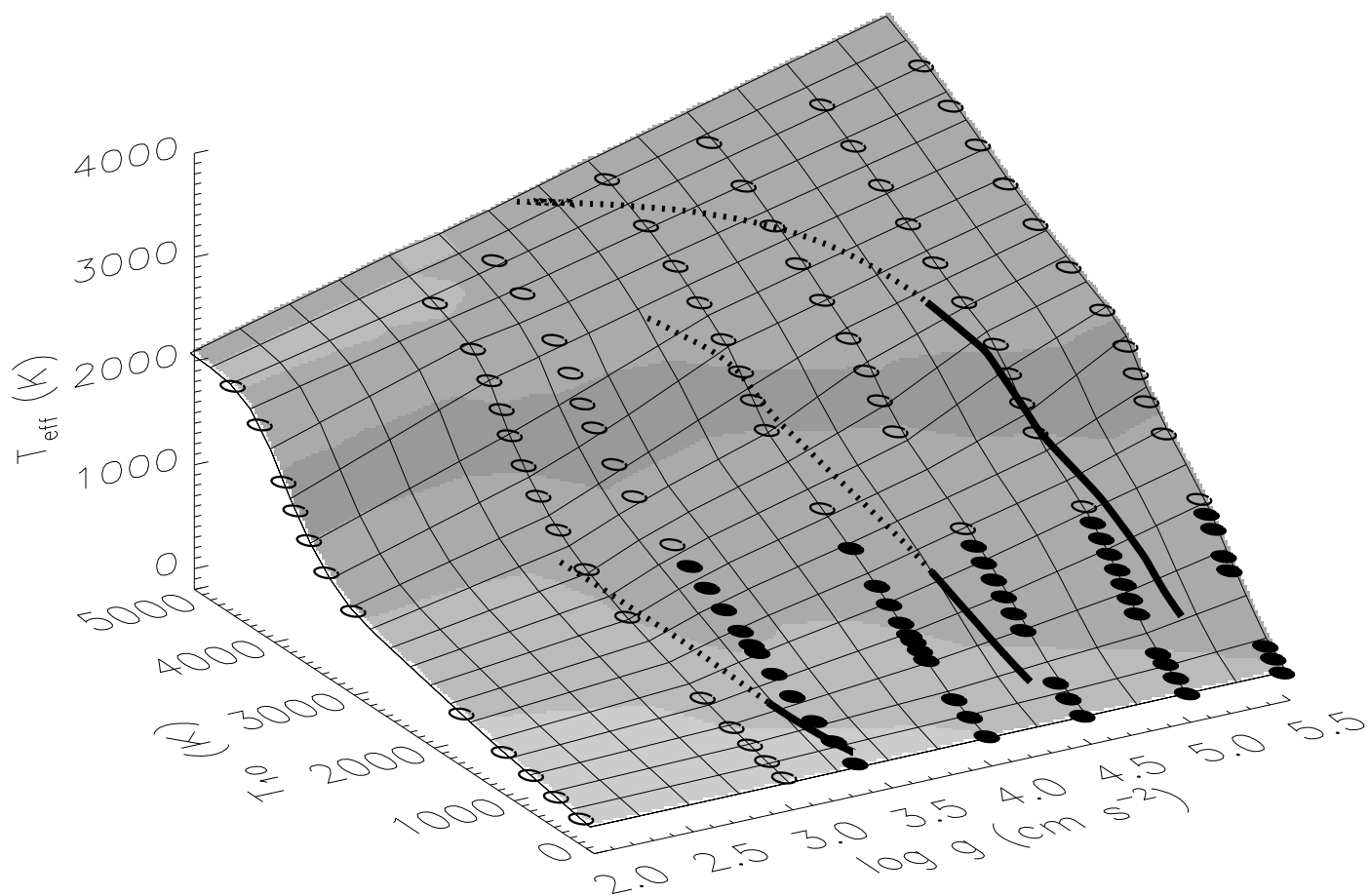
Fig. 22.— Absolute J vs. $J - H$ color–magnitude diagram. Otherwise as in Figure 20.

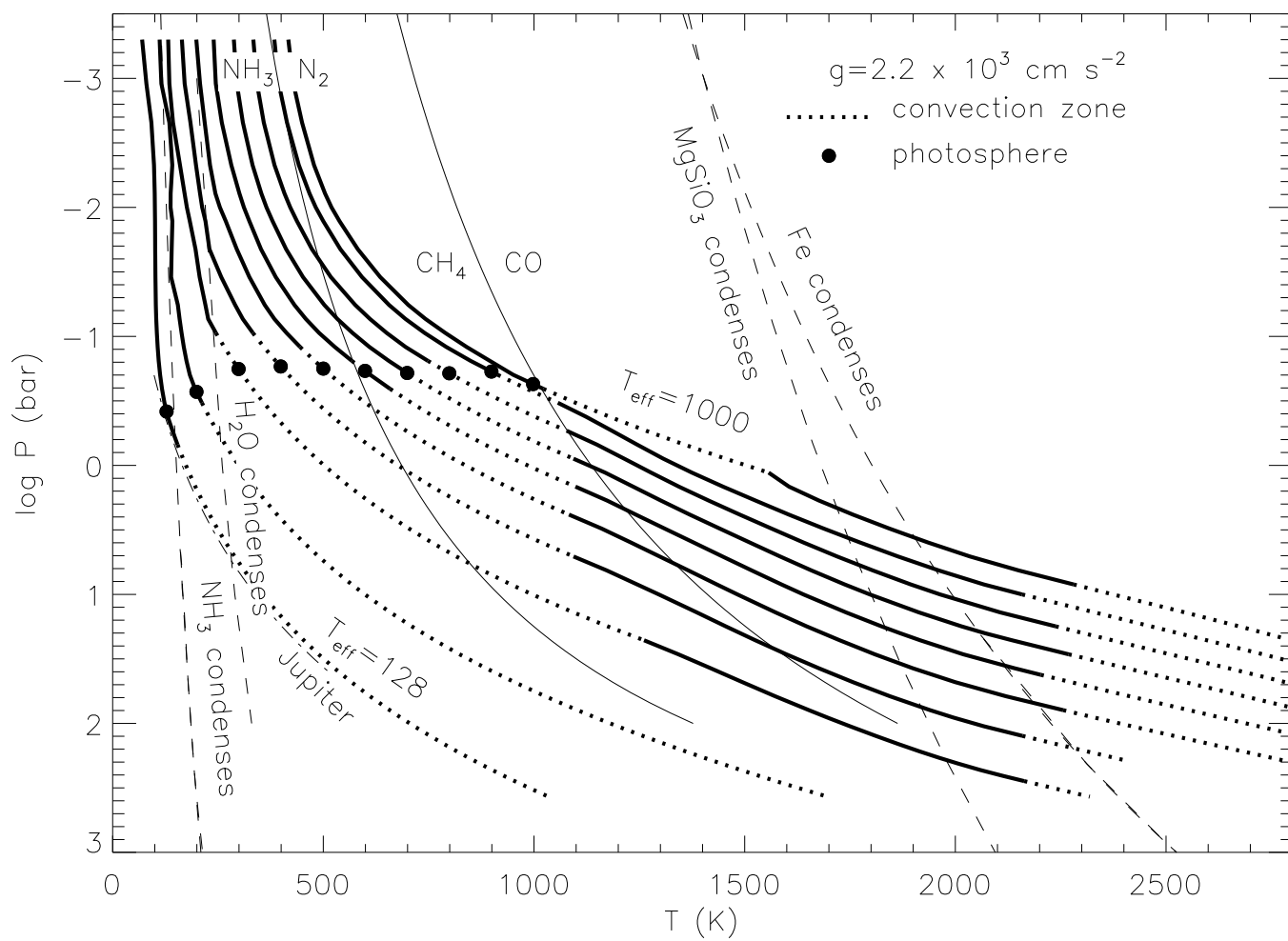
Fig. 23.— Absolute H vs. $J - H$ color–magnitude diagram. Otherwise as in Figure 20.

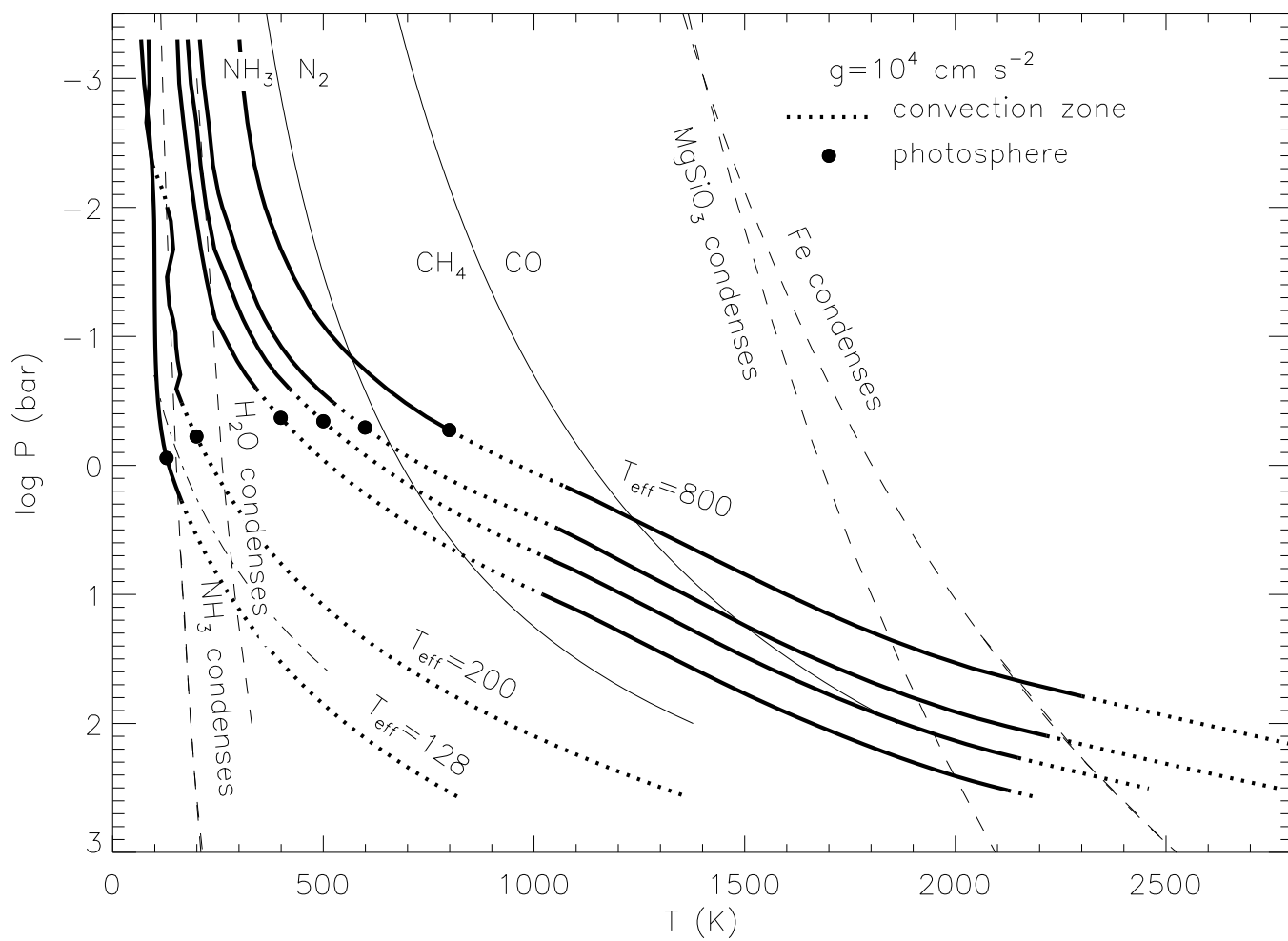
Fig. 24.— Absolute H vs. $H - K$ color–magnitude diagram. Otherwise as in Figure 20.

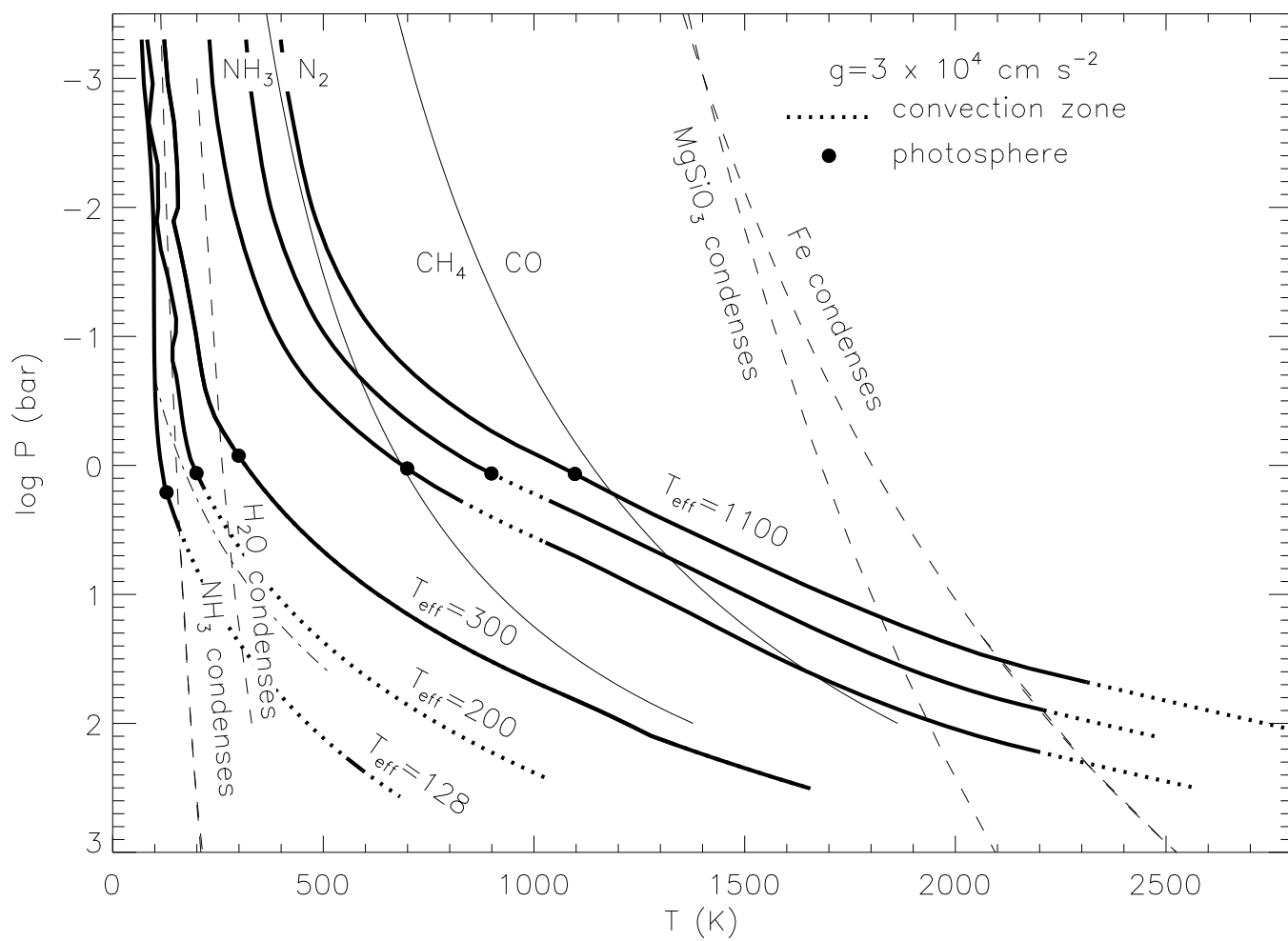
Fig. 25.— $J - H$ vs. $H - K$ color–color diagram. The edge of the main sequence as a function of metallicity, from our calculations employing Allard & Hauschildt (1995) atmosphere models, is shown for metallicities from $[M/H]=0$ (top) to $[M/H]=-3$ (bottom) (Saumon *et al.* in preparation). Otherwise as in Figure 20.

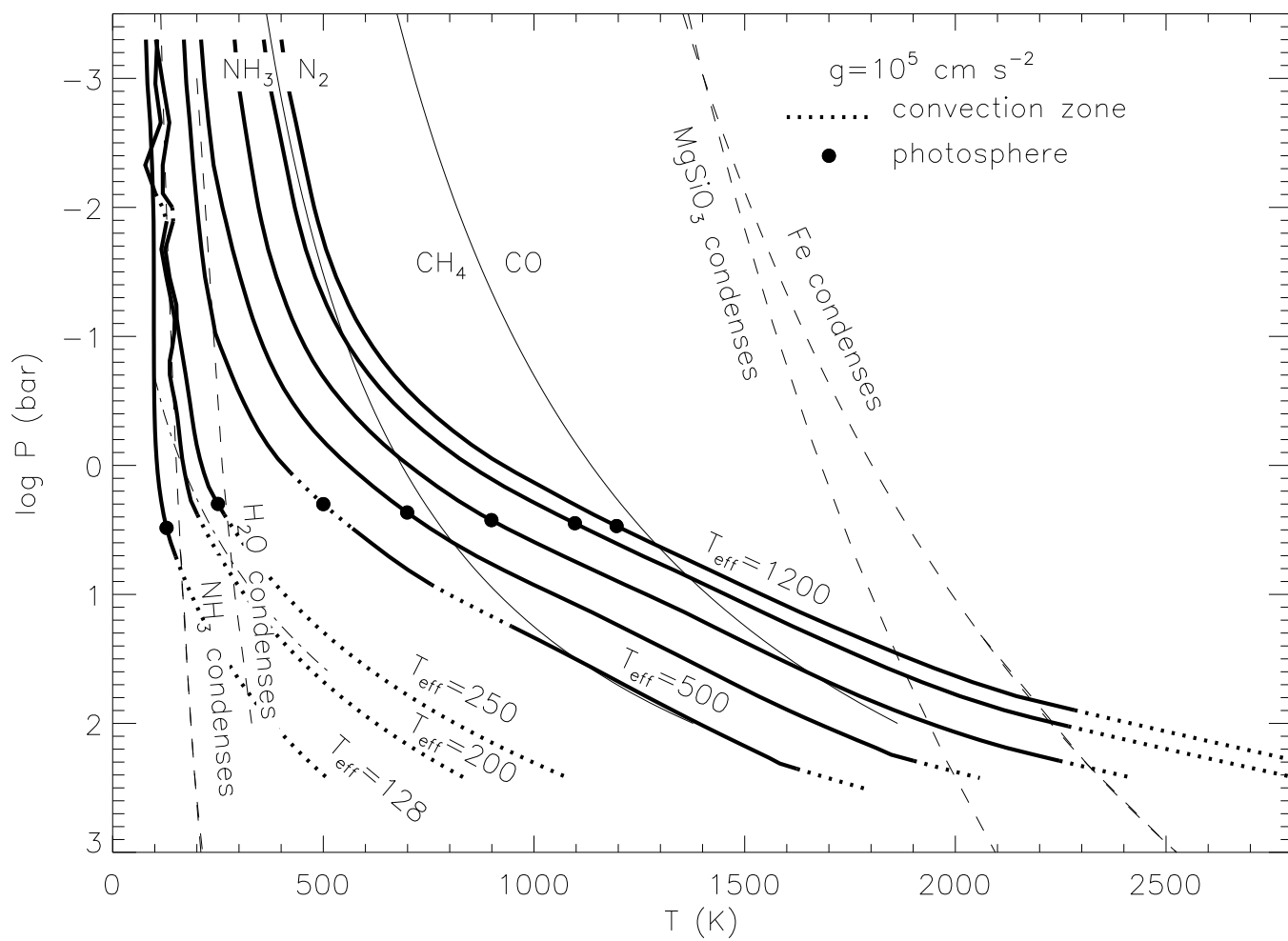
Fig. 26.— $J - K$ vs. $K - L'$ color–color diagram. Otherwise as in Figure 25.

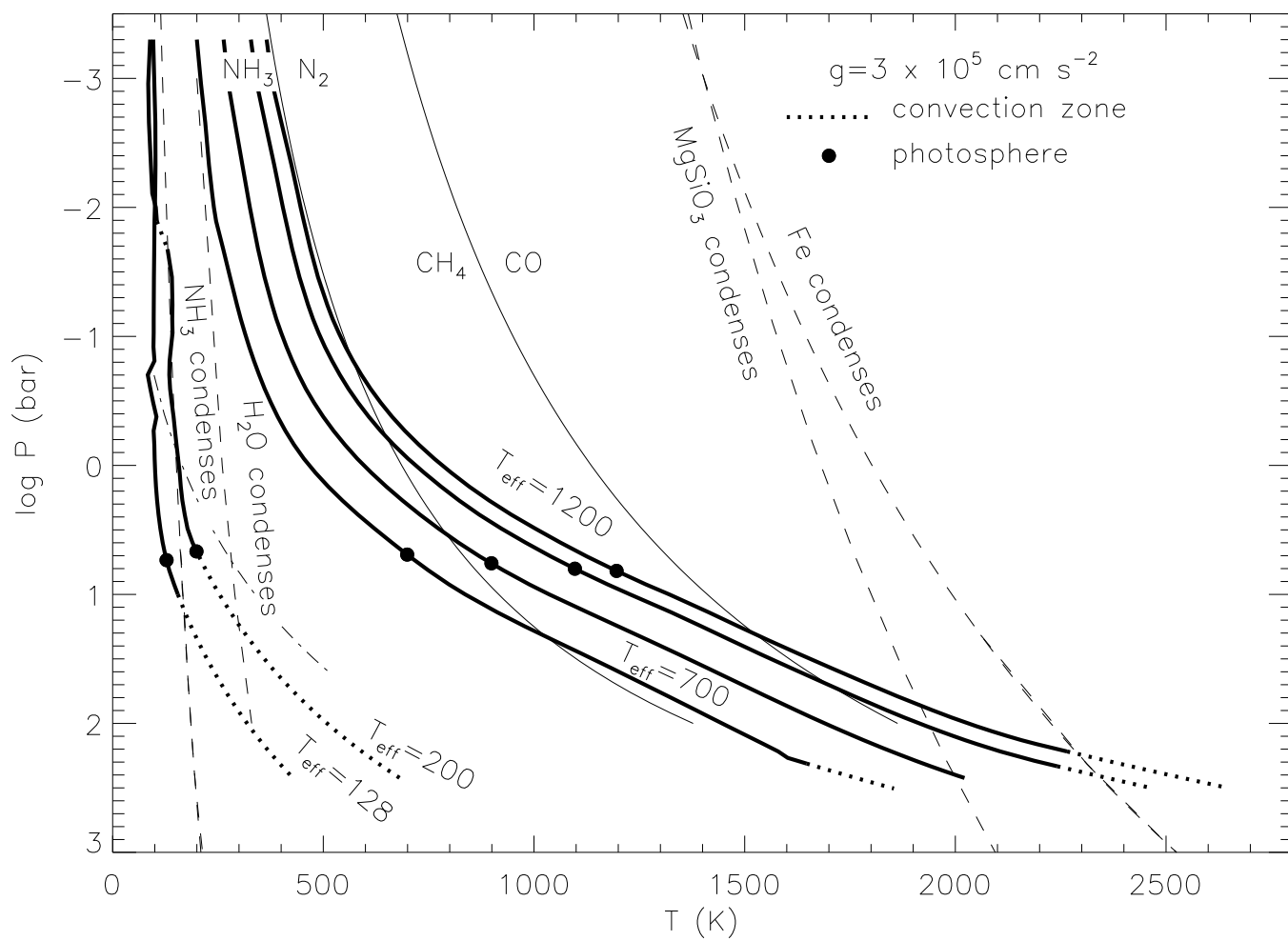


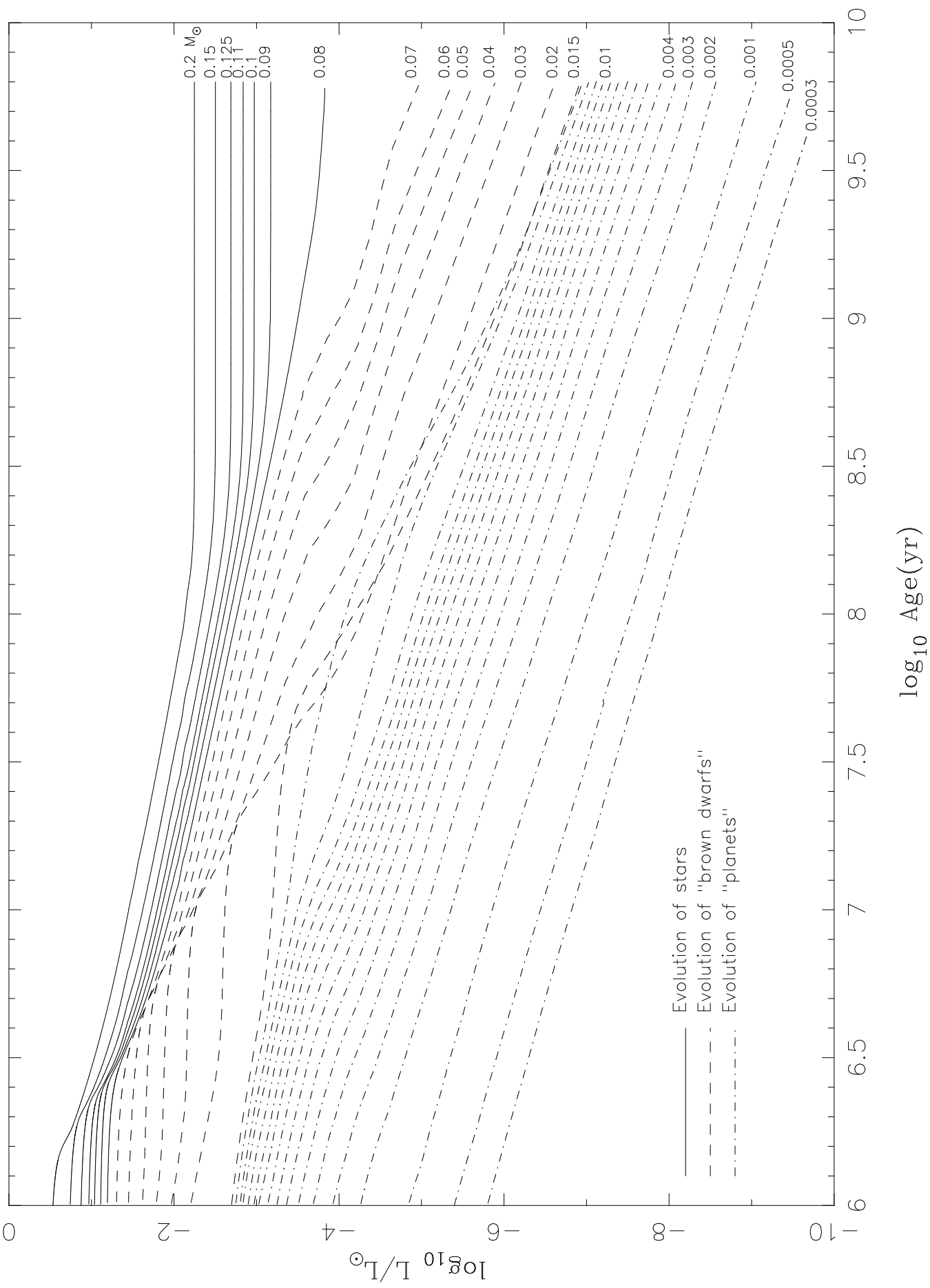


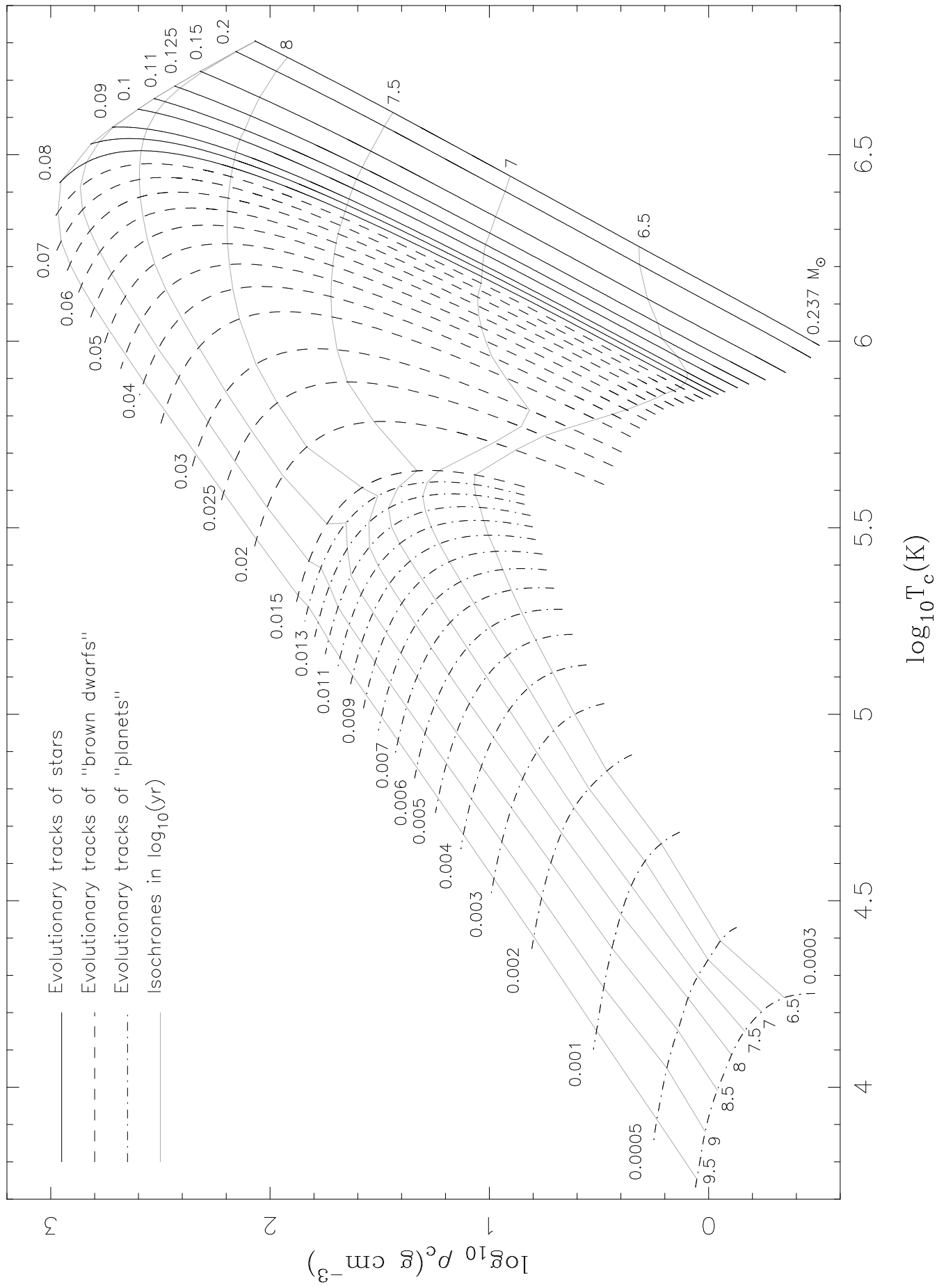


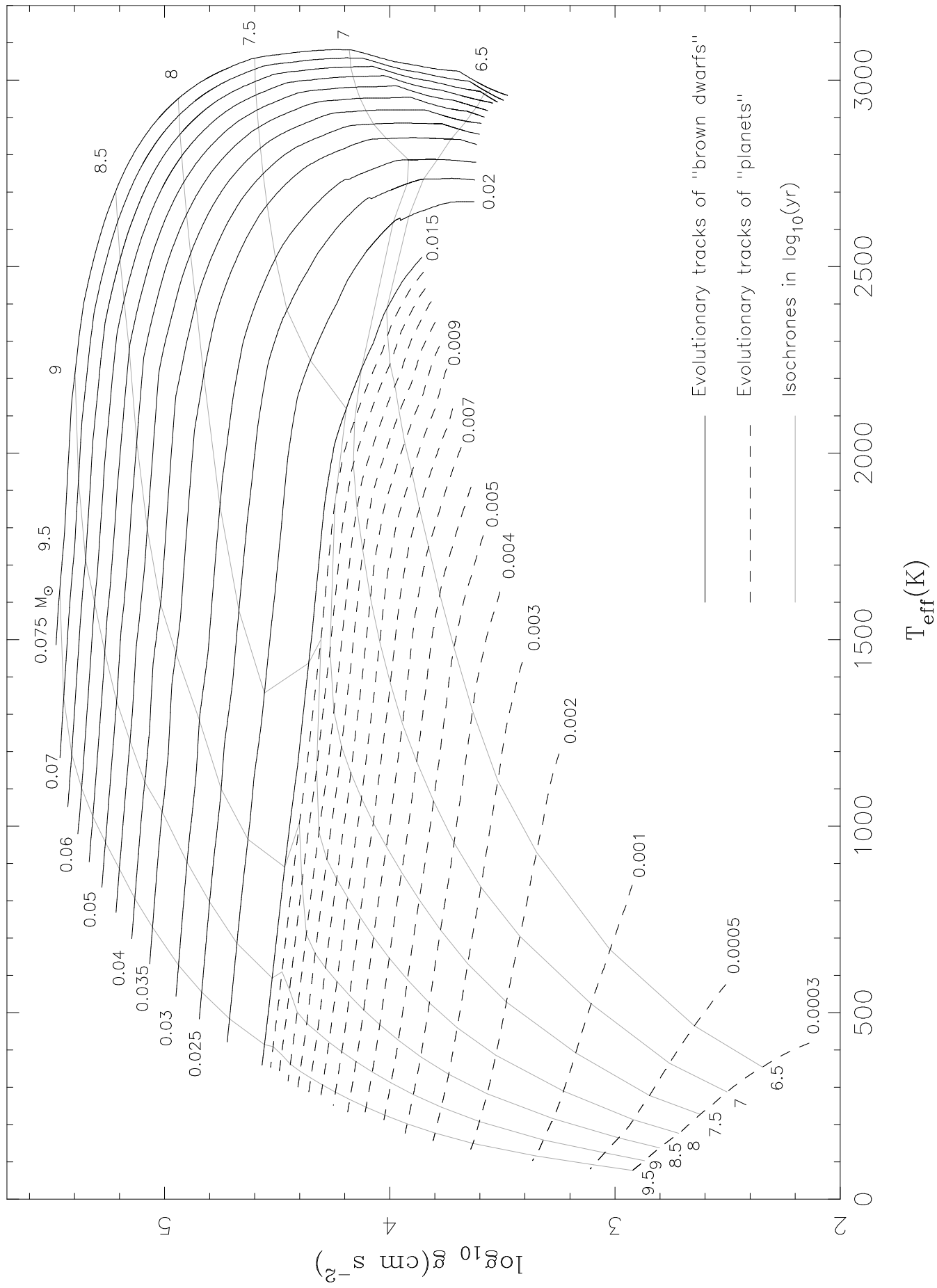


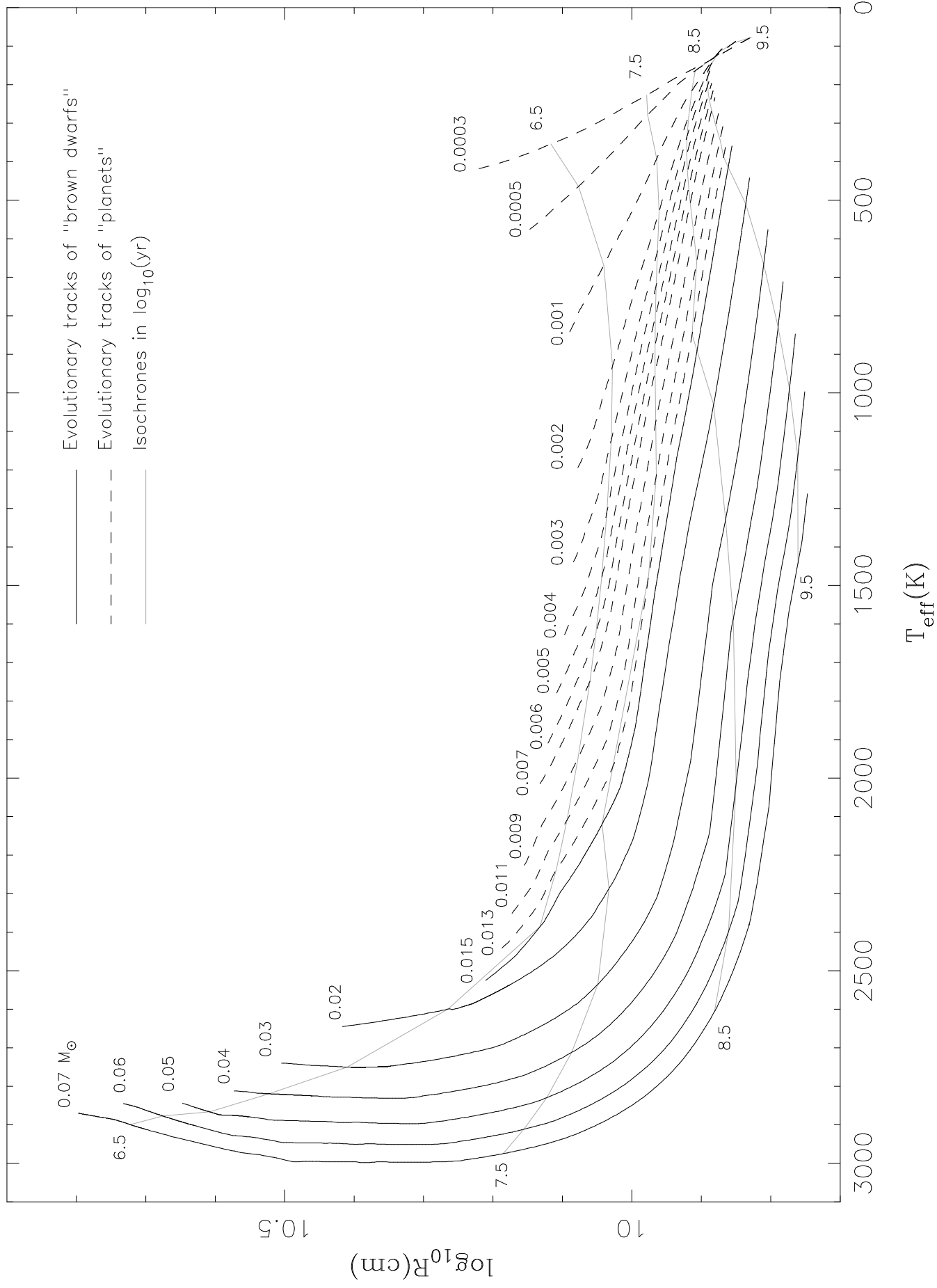


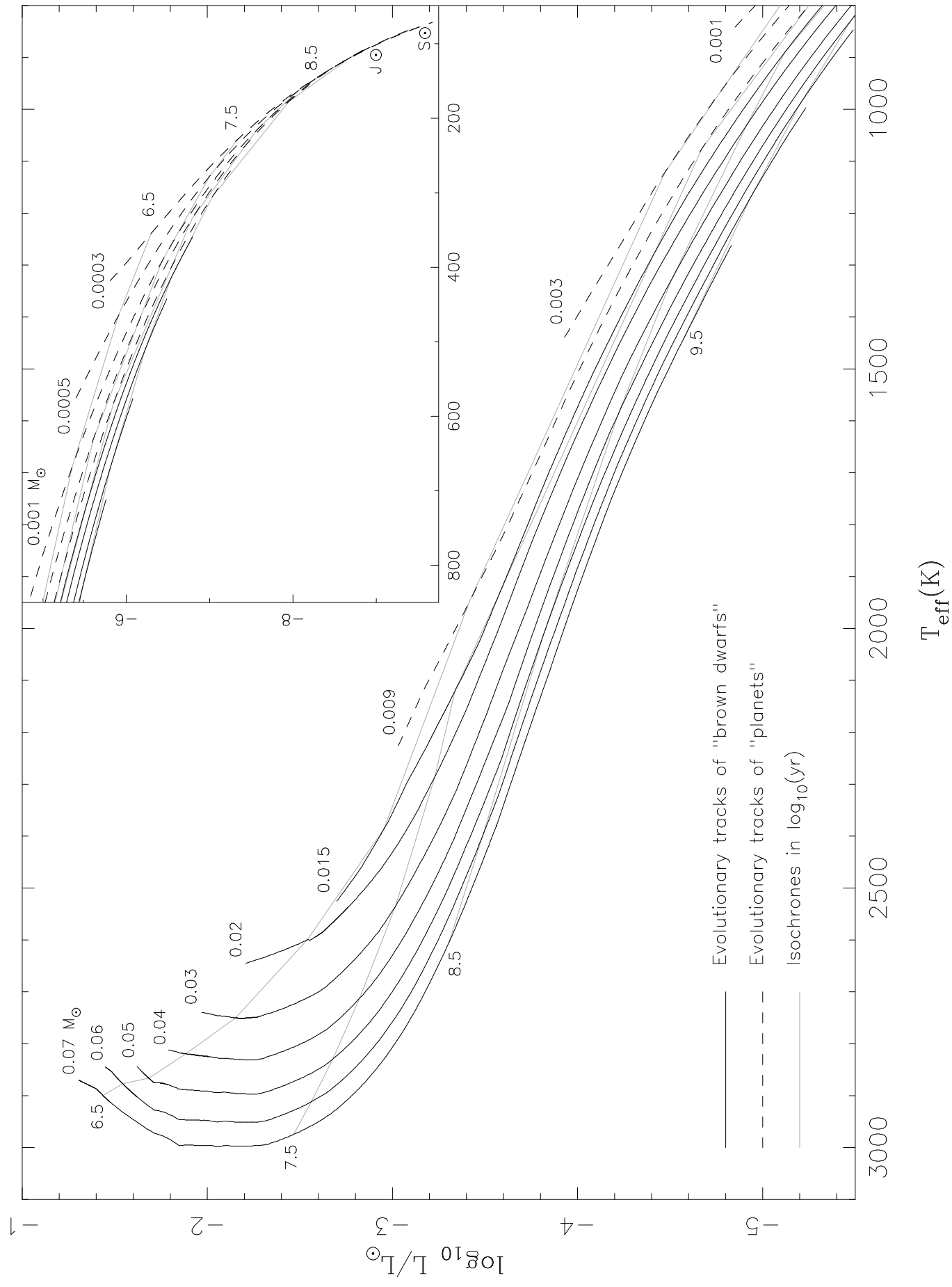


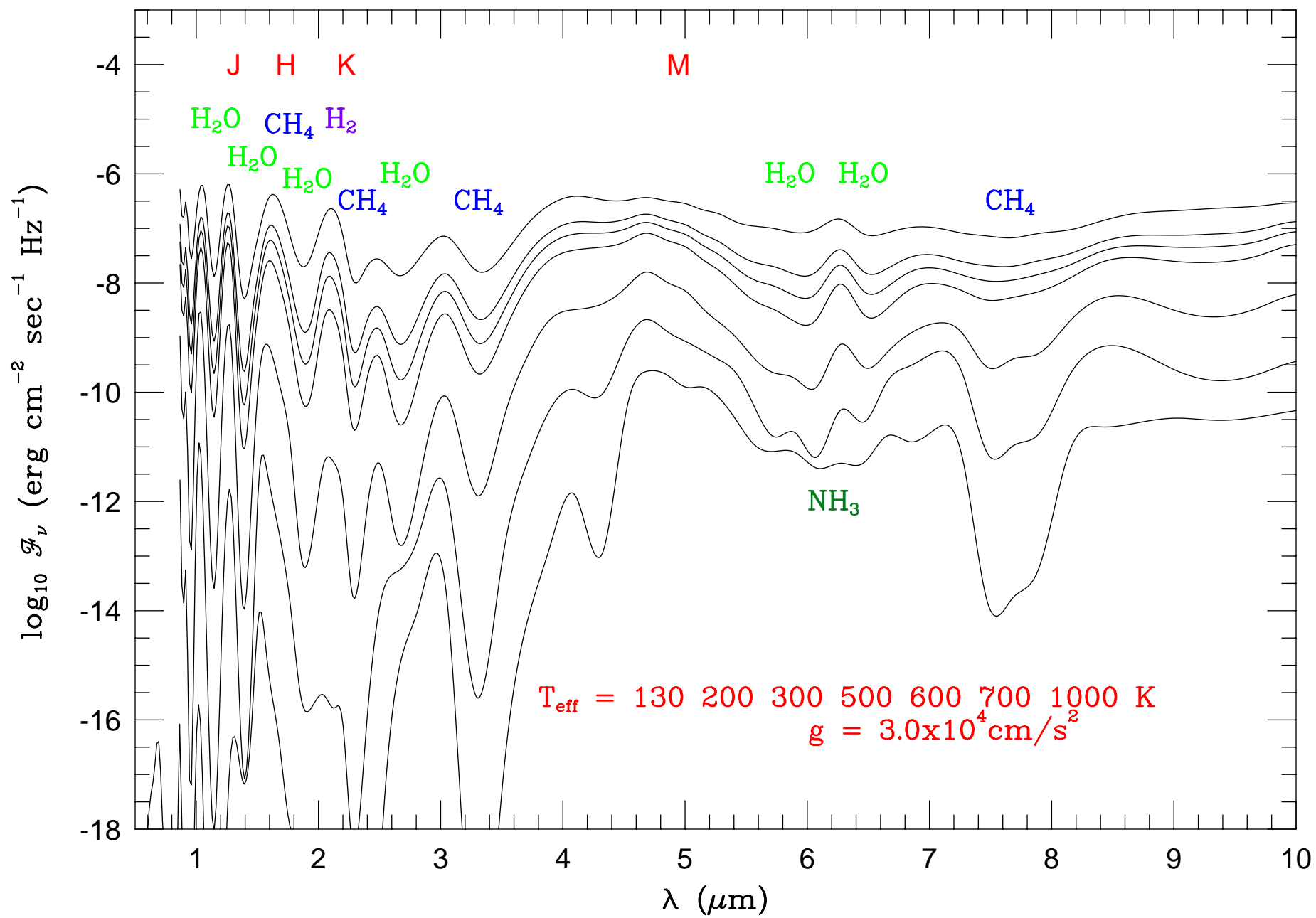


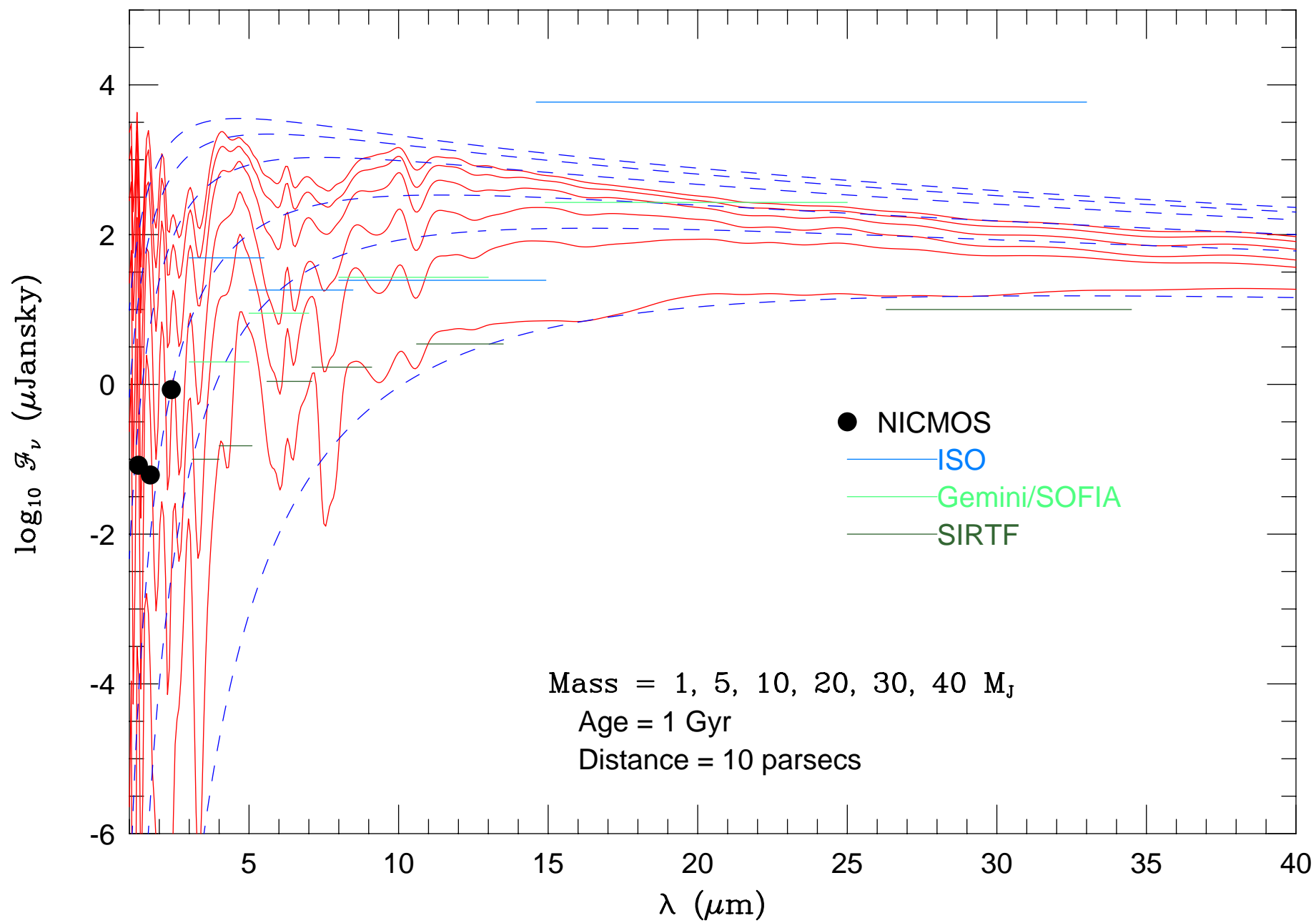


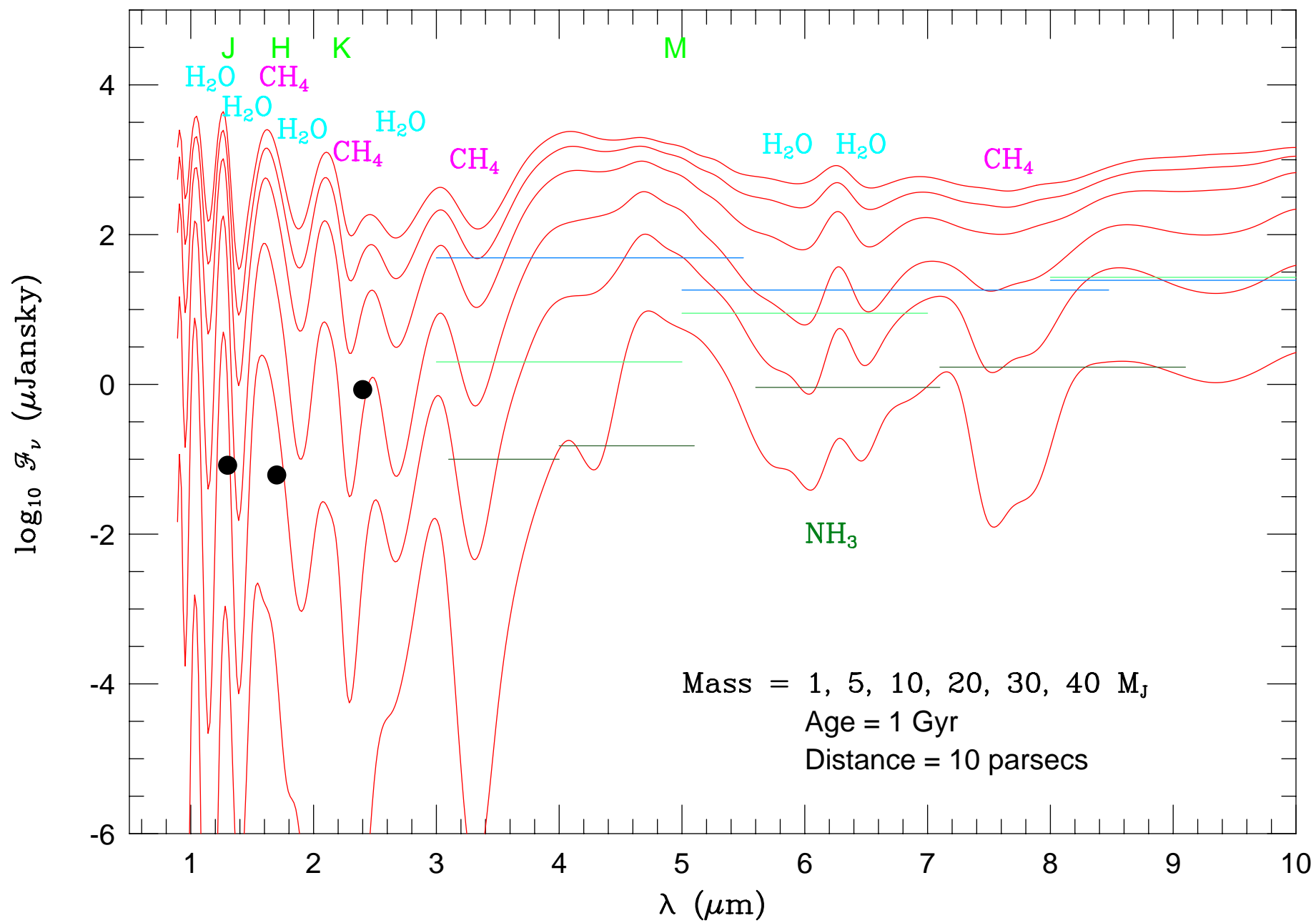


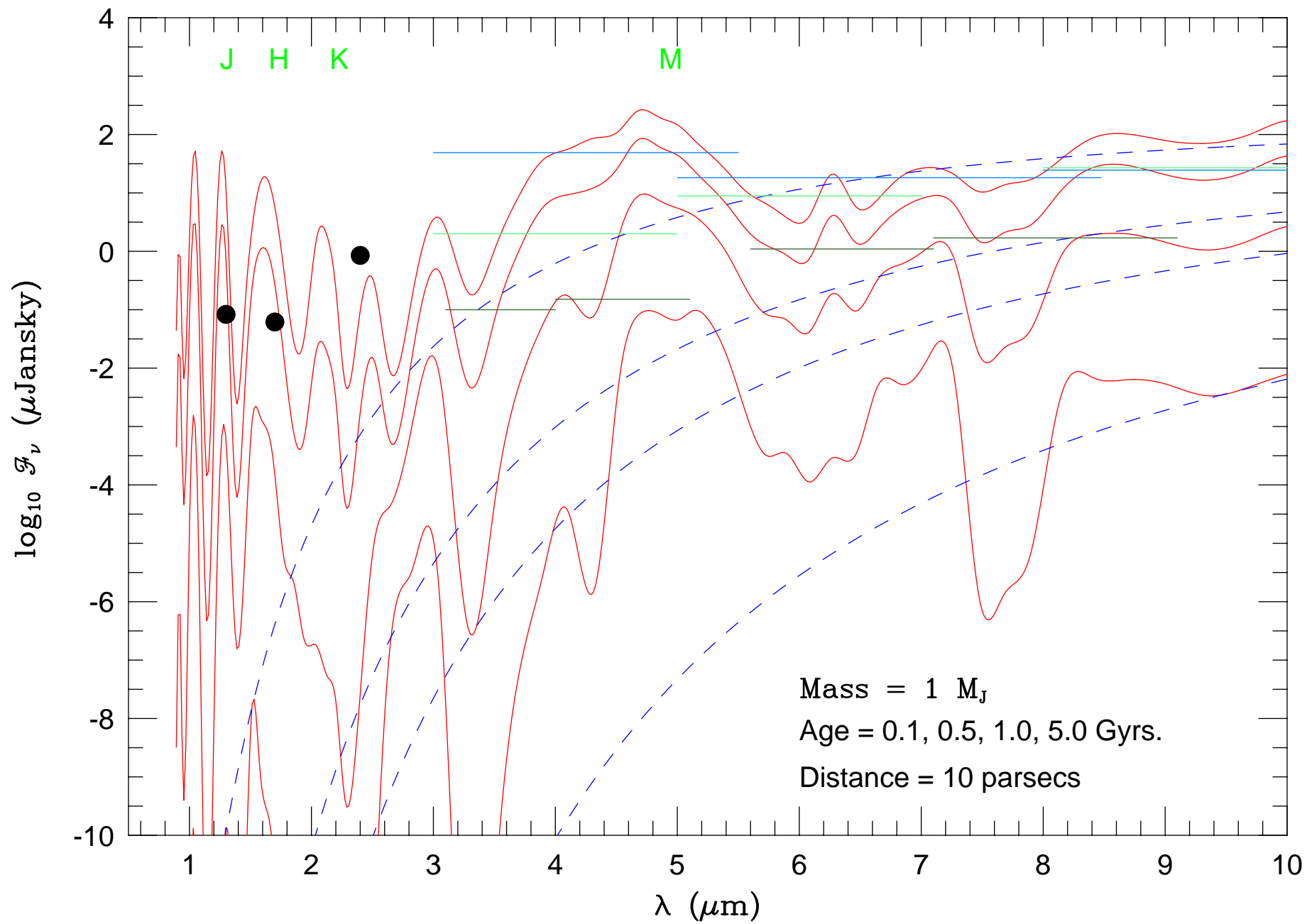


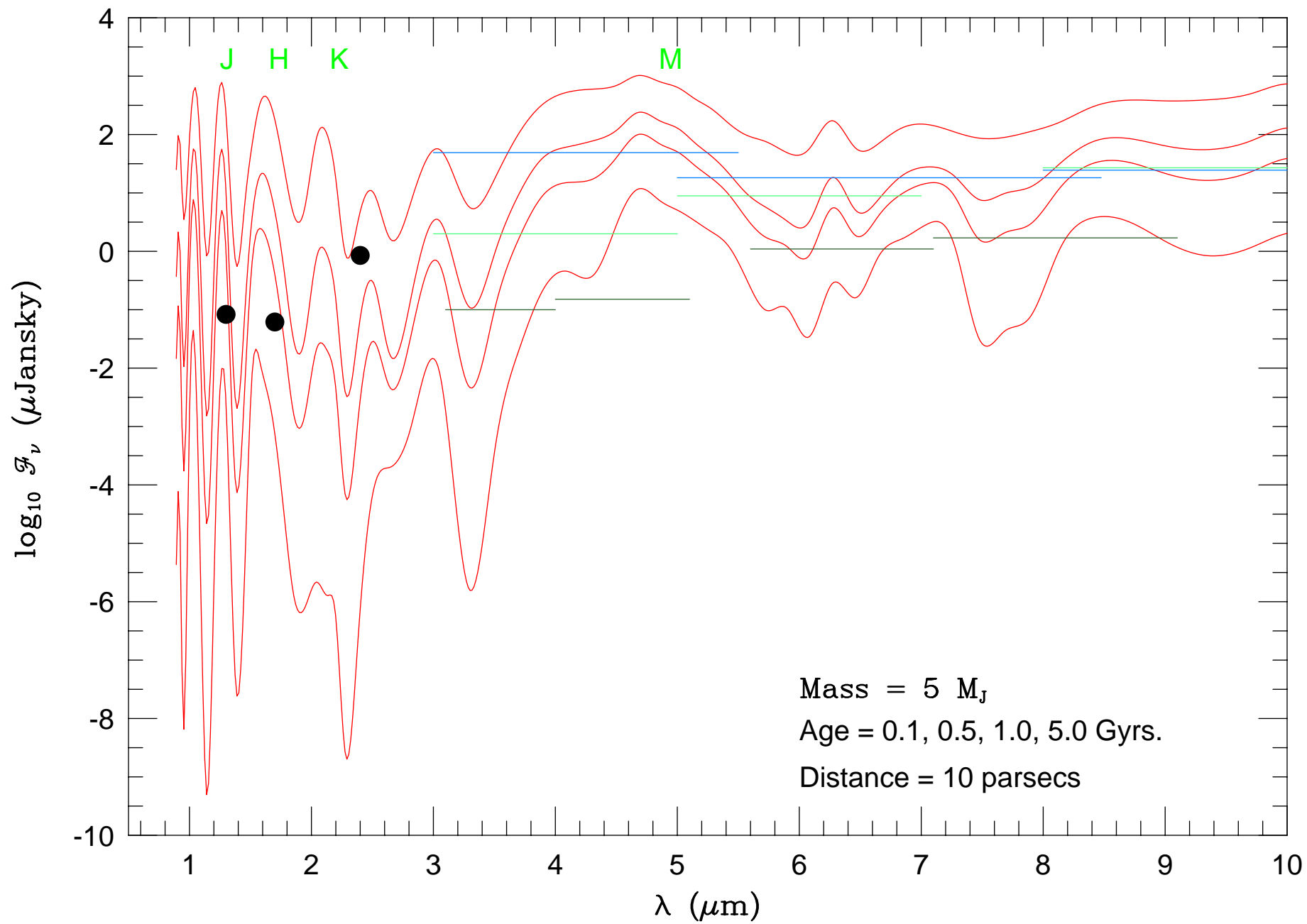


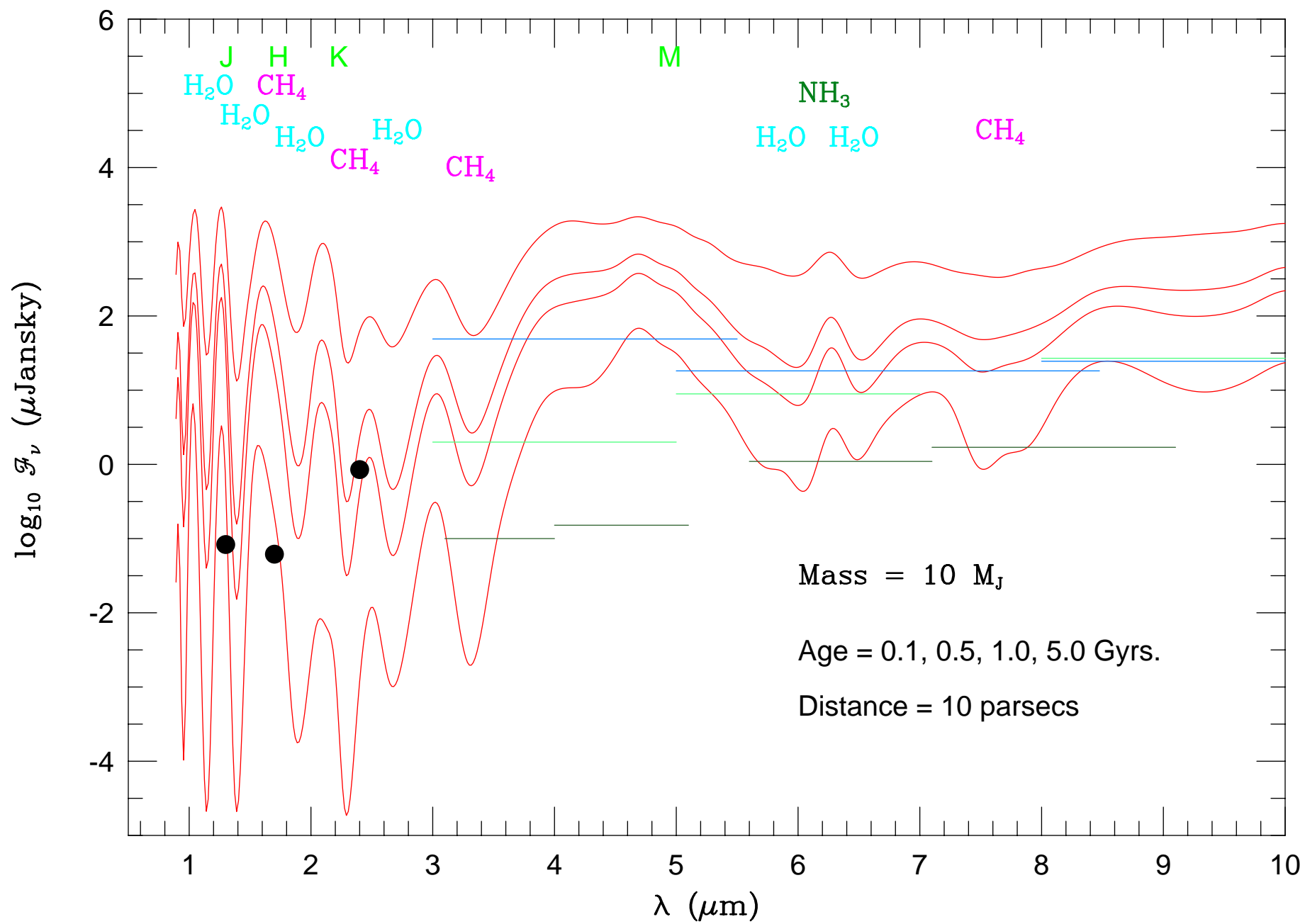


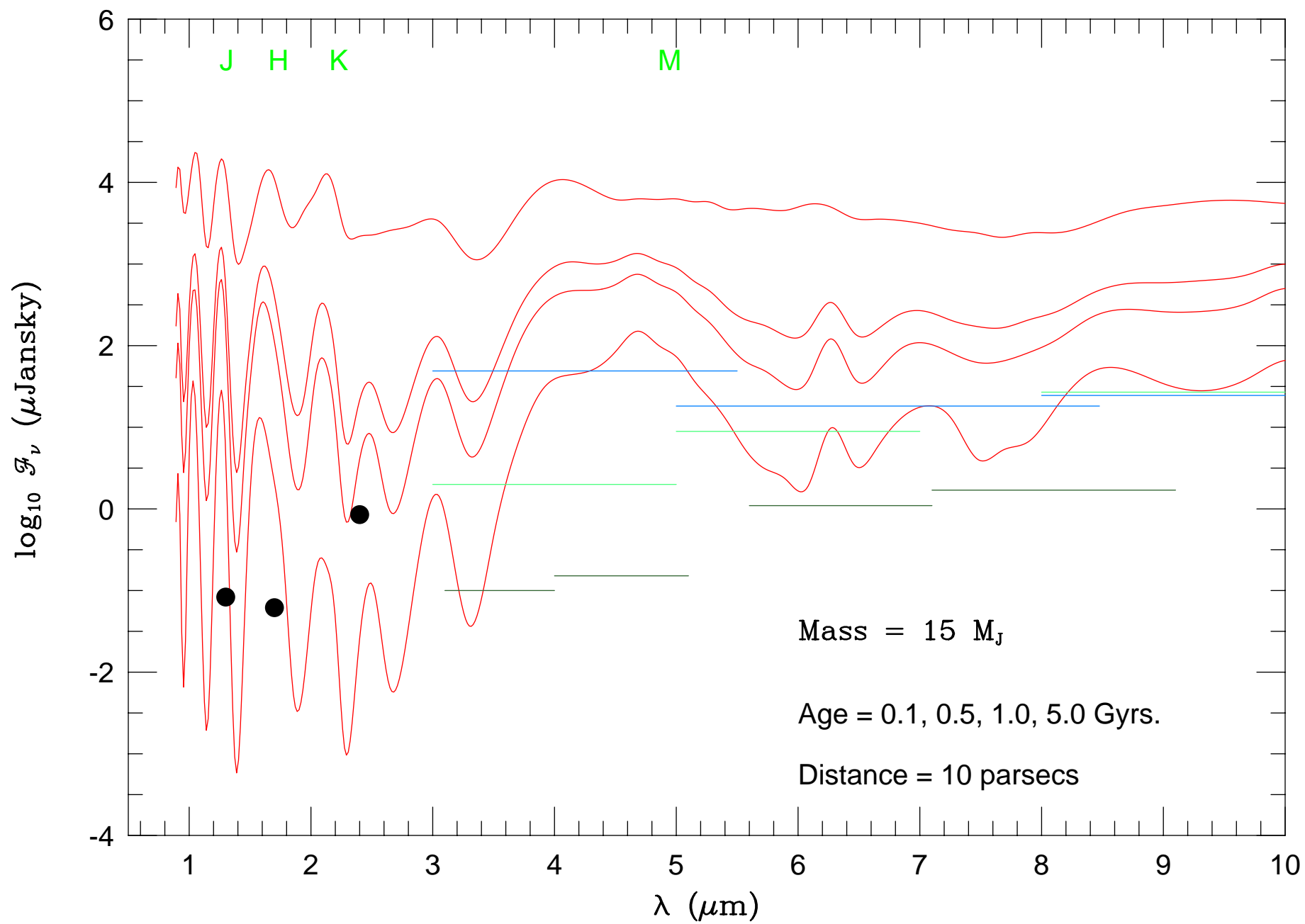


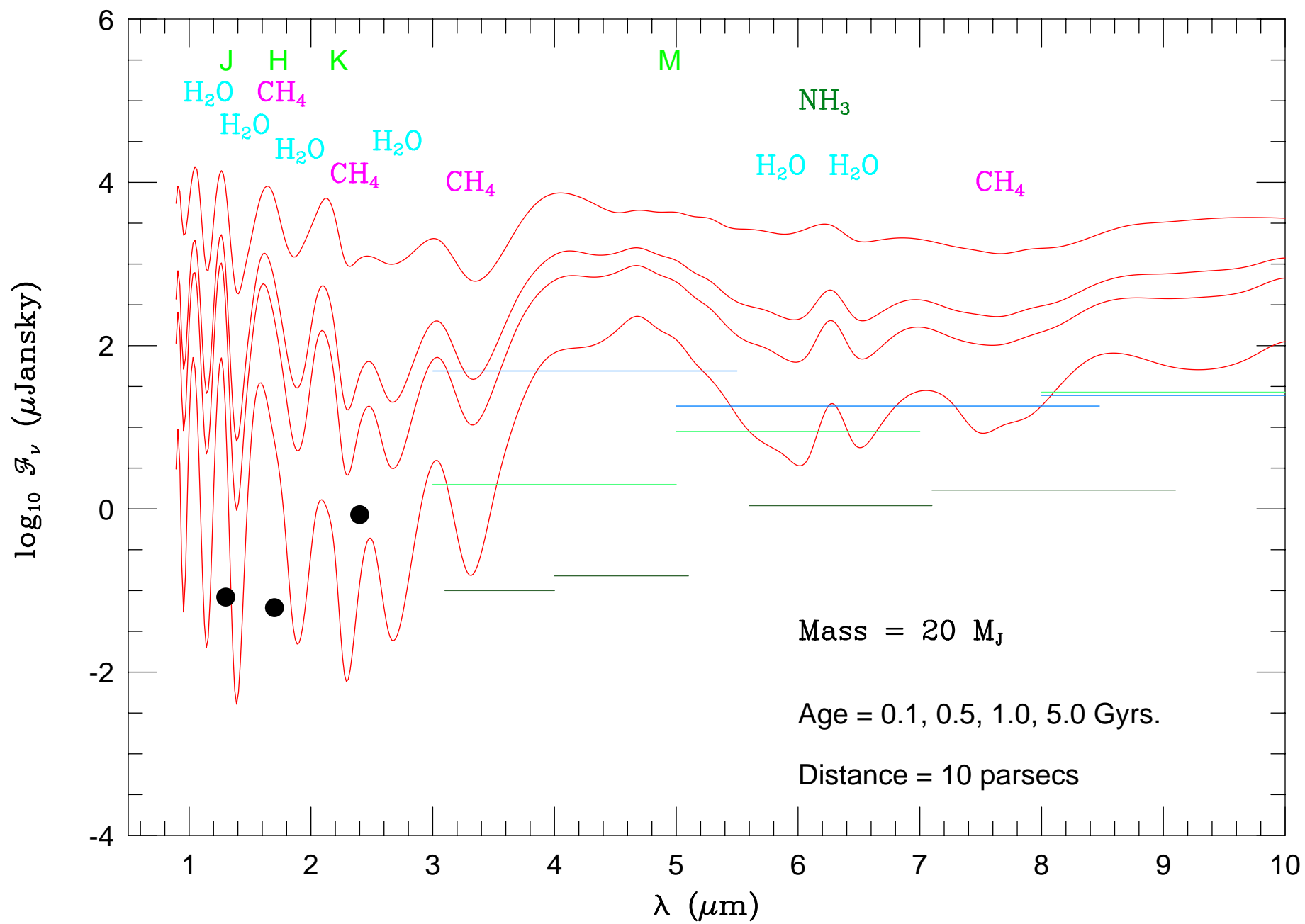


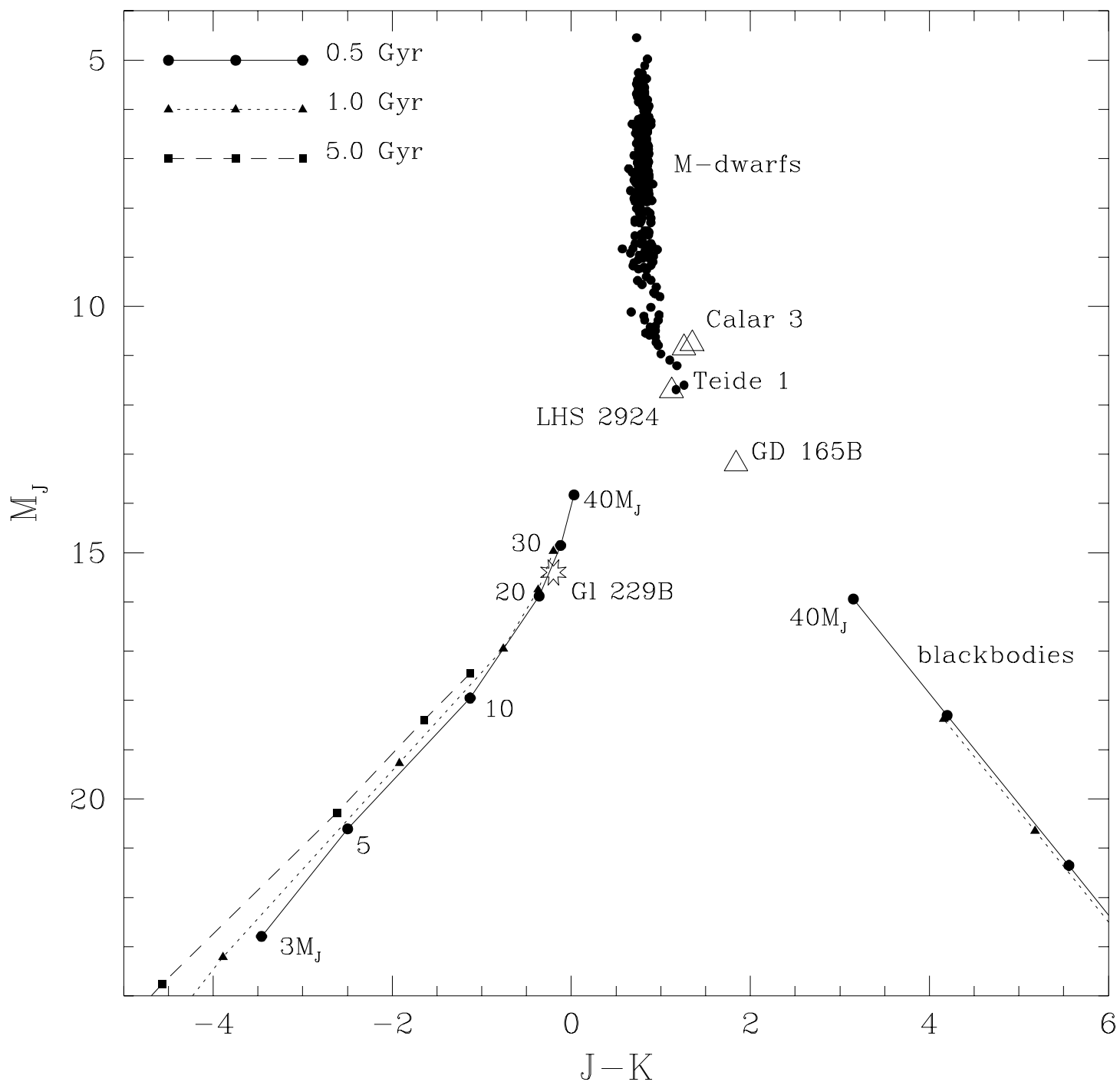


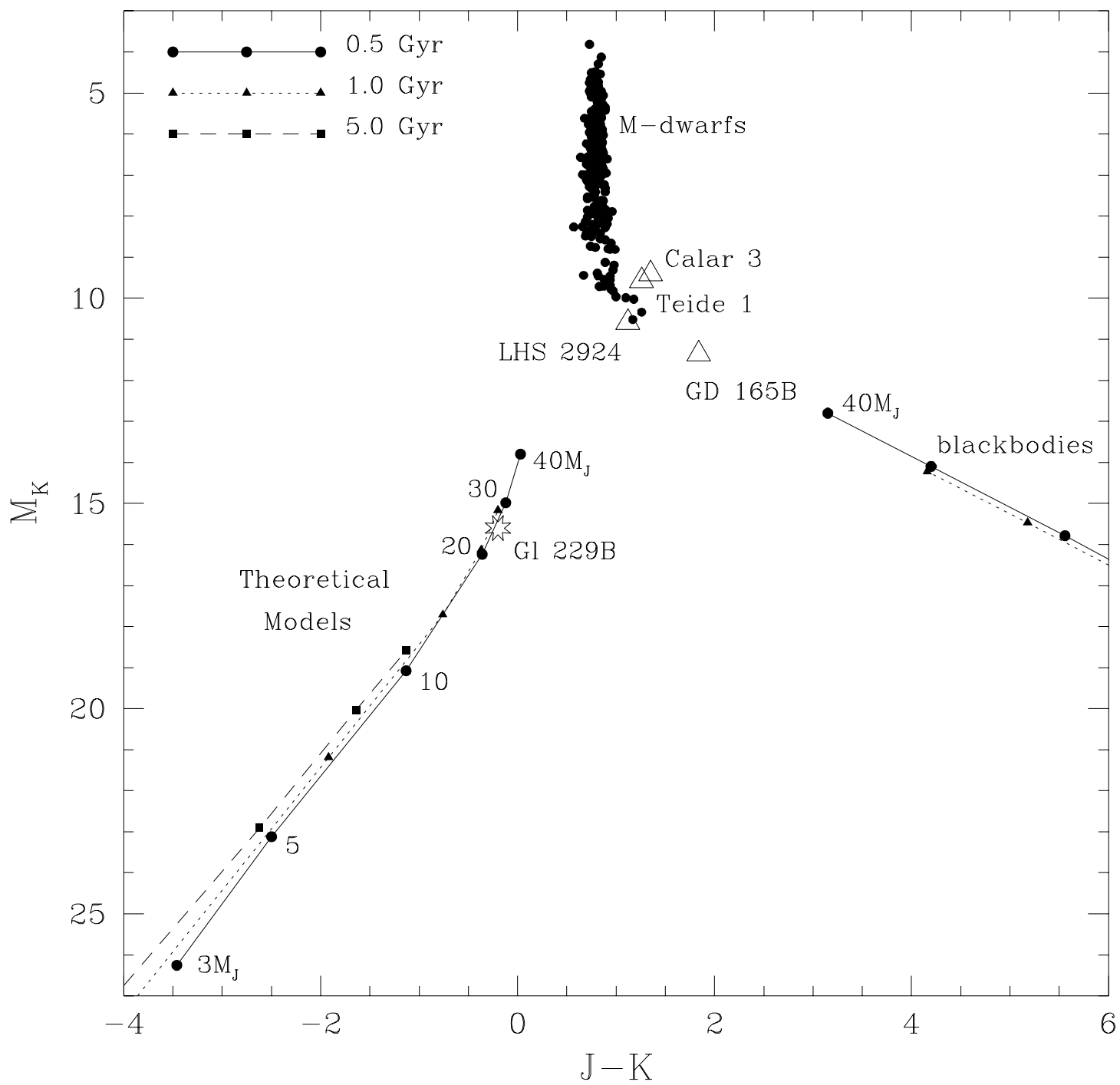


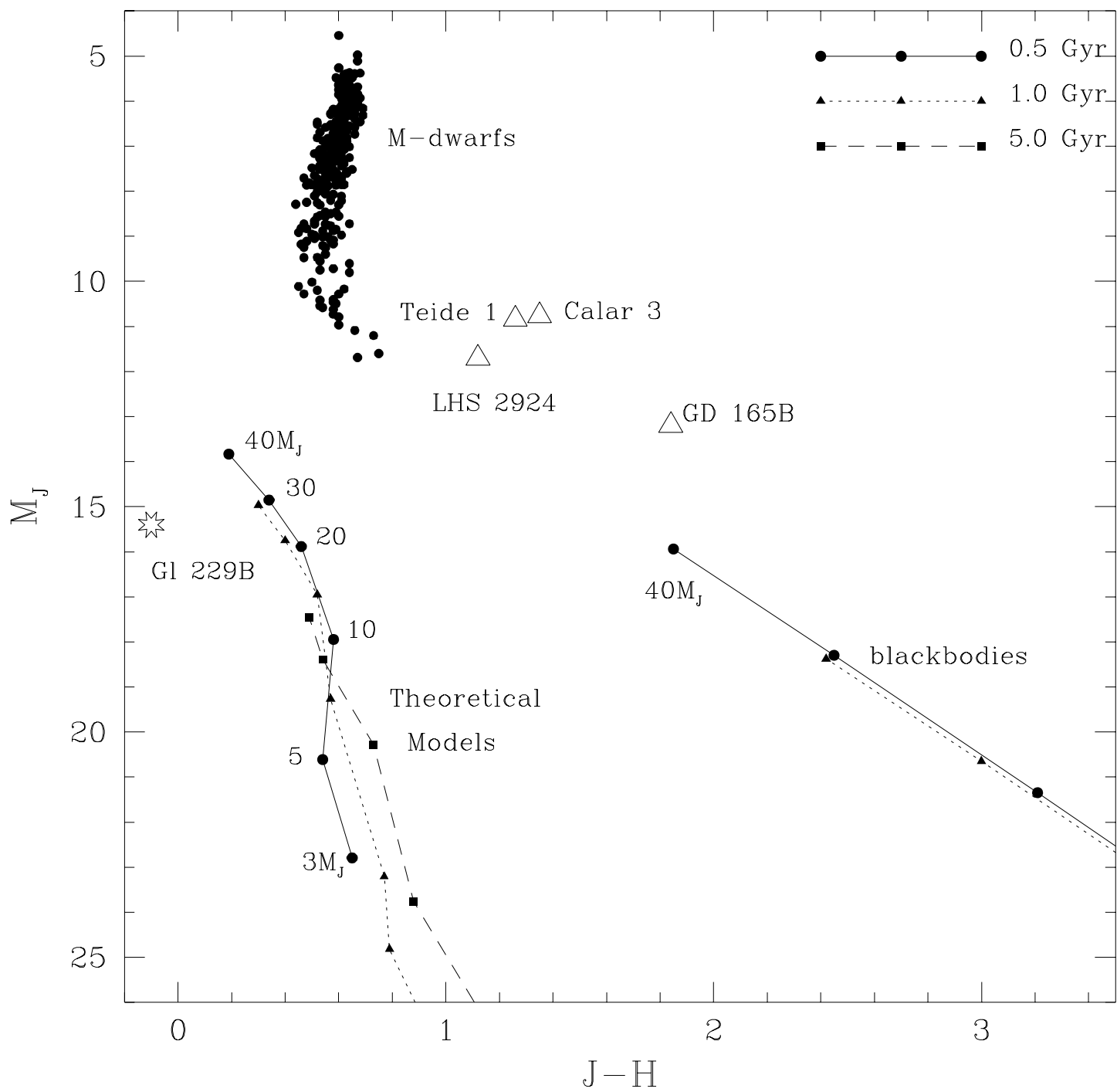


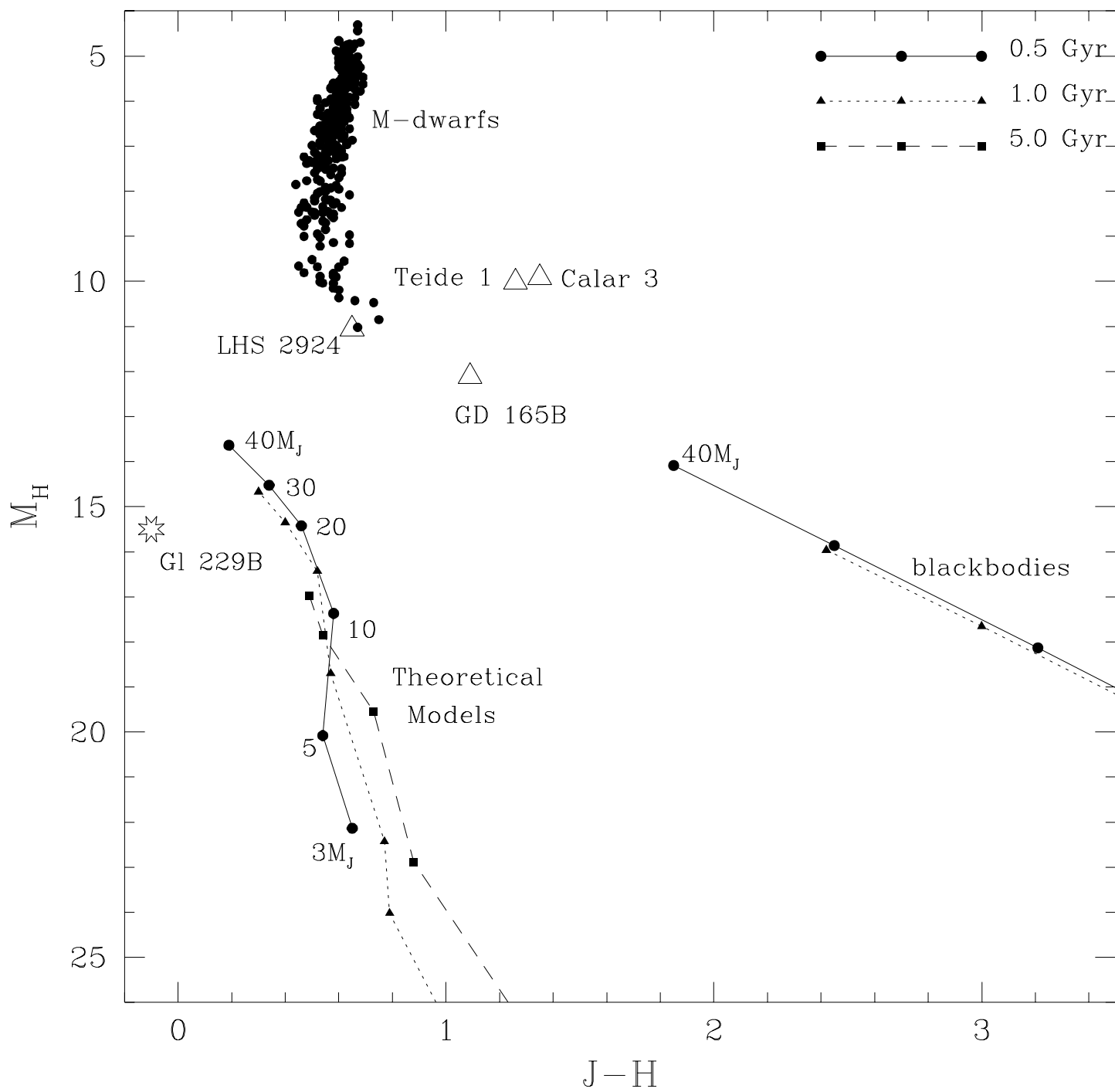


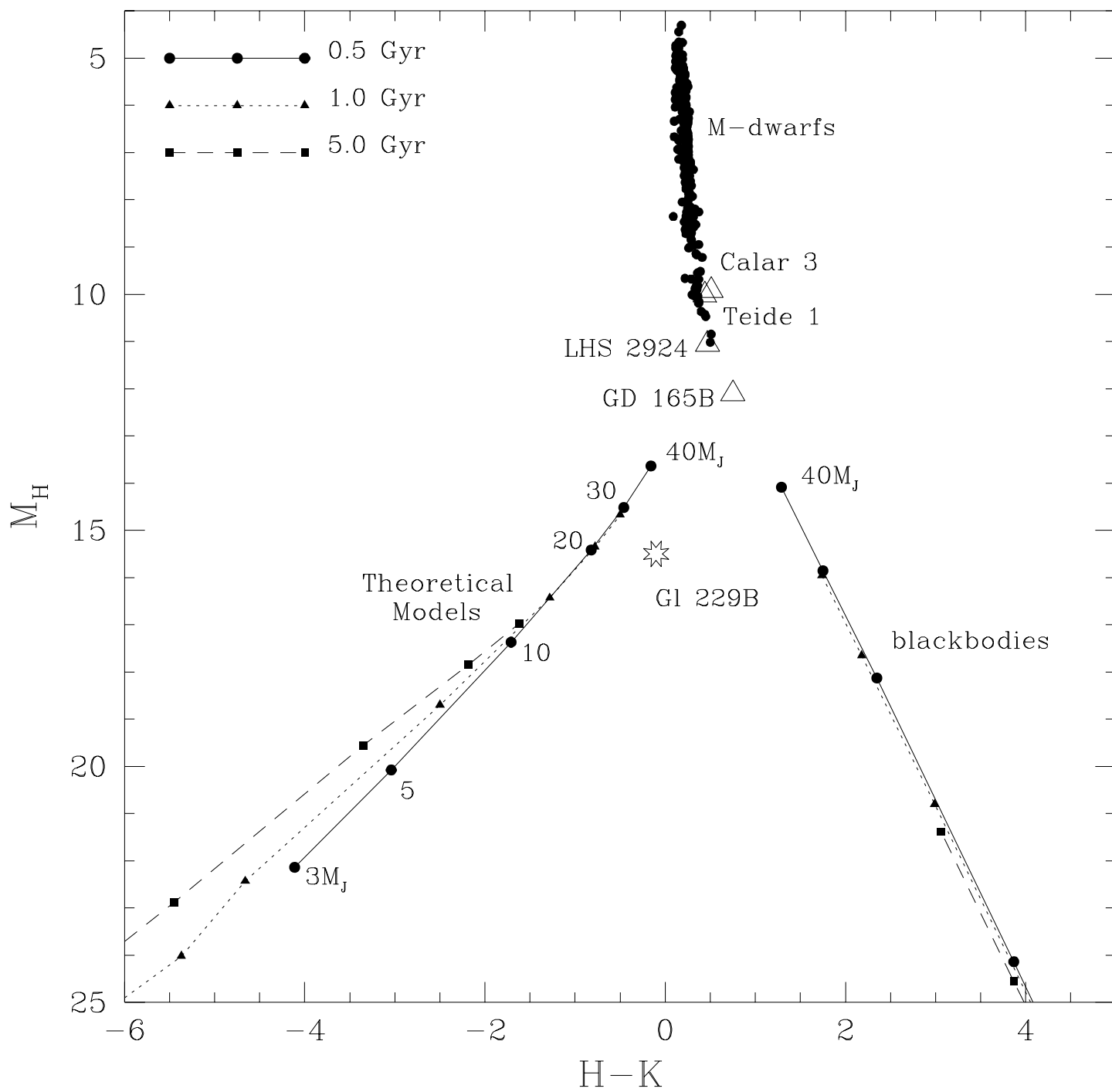


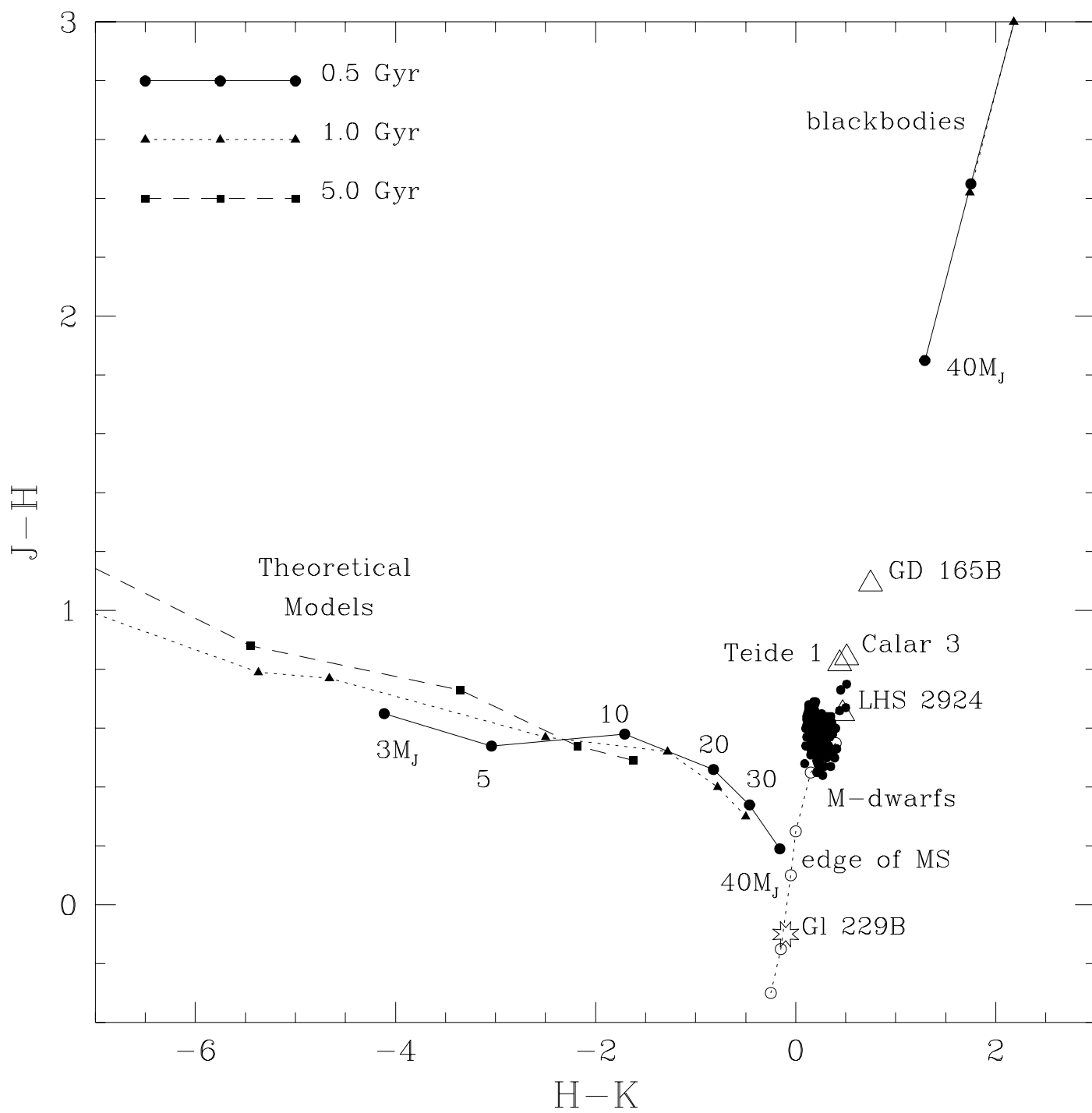












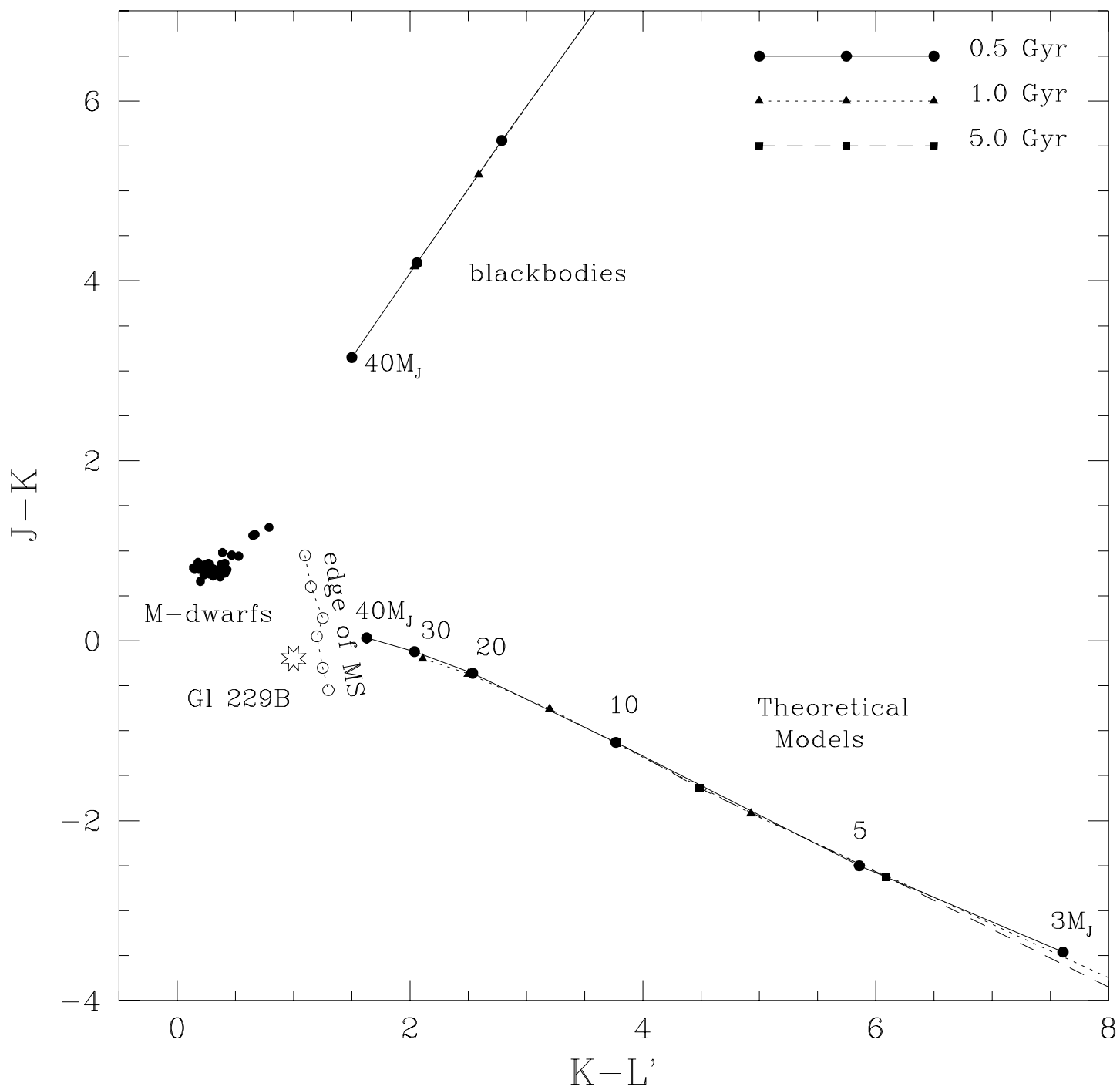


Table 1a. Evolution of a 1 M_J planet

$\log t$ (Gyr)	T_{eff} (K)	$\log L/L_{\odot}$	R (10^9 cm)	$\log T_c$ (K)	$\log \rho_c$ (g cm ⁻³)	L_{nuclear}/L
−2.990	839.9	−4.851	12.33	4.684	0.130	0.000
−2.780	767.4	−5.053	11.70	4.673	0.168	0.000
−2.567	699.7	−5.257	11.13	4.658	0.205	0.000
−2.365	631.7	−5.474	10.64	4.641	0.239	0.000
−2.156	575.9	−5.671	10.20	4.620	0.272	0.000
−1.944	515.5	−5.898	9.81	4.595	0.303	0.000
−1.734	455.1	−6.145	9.47	4.567	0.331	0.000
−1.520	397.6	−6.407	9.17	4.536	0.356	0.000
−1.312	347.5	−6.664	8.93	4.505	0.377	0.000
−1.101	304.0	−6.919	8.71	4.474	0.394	0.000
−0.898	267.9	−7.157	8.53	4.442	0.410	0.000
−0.682	235.9	−7.397	8.34	4.406	0.427	0.000
−0.474	209.0	−7.625	8.18	4.367	0.443	0.000
−0.261	184.8	−7.856	8.01	4.326	0.459	0.000
−0.050	163.9	−8.081	7.86	4.283	0.474	0.000
0.155	145.3	−8.306	7.71	4.236	0.488	0.000
0.363	128.1	−8.541	7.58	4.185	0.502	0.000
0.571	112.4	−8.783	7.45	4.132	0.517	0.000
0.778	98.9	−9.020	7.33	4.076	0.532	0.000
0.982	86.4	−9.268	7.22	4.016	0.547	0.000

Table 1b. Evolution of a 5 M_J planet

$\log t$ (Gyr)	T_{eff} (K)	$\log L/L_{\odot}$	R (10^9 cm)	$\log T_c$ (K)	$\log \rho_c$ (g cm^{-3})	L_{nuclear}/L
−2.998	1814.0	−3.482	12.79	5.214	0.625	0.000
−2.792	1689.0	−3.664	11.96	5.211	0.699	0.000
−2.582	1494.0	−3.929	11.26	5.202	0.767	0.000
−2.380	1352.0	−4.144	10.74	5.191	0.824	0.000
−2.176	1228.0	−4.351	10.26	5.173	0.880	0.000
−1.973	1094.0	−4.587	9.85	5.151	0.932	0.000
−1.772	967.3	−4.832	9.50	5.125	0.978	0.000
−1.571	848.7	−5.086	9.22	5.097	1.018	0.000
−1.368	740.6	−5.345	8.98	5.067	1.053	0.000
−1.163	643.8	−5.609	8.77	5.038	1.083	0.000
−0.961	561.6	−5.863	8.60	5.009	1.108	0.000
−0.749	489.0	−6.120	8.44	4.978	1.131	0.000
−0.534	424.8	−6.379	8.30	4.947	1.152	0.000
−0.332	373.1	−6.617	8.18	4.917	1.170	0.000
−0.131	327.9	−6.853	8.07	4.886	1.186	0.000
0.083	285.4	−7.105	7.96	4.853	1.202	0.000
0.297	248.5	−7.356	7.87	4.819	1.216	0.000
0.502	218.3	−7.591	7.79	4.786	1.229	0.000
0.712	193.2	−7.812	7.71	4.750	1.241	0.000
0.920	172.8	−8.015	7.63	4.711	1.253	0.000

Table 1c. Evolution of a 10 M_J planet/Brown dwarf

$\log t$ (Gyr)	T_{eff} (K)	$\log L/L_{\odot}$	R (10^9 cm)	$\log T_c$ (K)	$\log \rho_c$ (g cm ⁻³)	L_{nuclear}/L
-2.987	2318.0	-2.934	14.72	5.466	0.772	0.000
-2.779	2238.0	-3.065	13.57	5.475	0.868	0.000
-2.572	2153.0	-3.208	12.44	5.480	0.975	0.001
-2.372	2006.0	-3.405	11.42	5.478	1.082	0.001
-2.165	1720.0	-3.732	10.66	5.468	1.170	0.003
-1.959	1539.0	-3.971	10.11	5.454	1.239	0.004
-1.750	1370.0	-4.214	9.64	5.435	1.302	0.005
-1.540	1221.0	-4.452	9.24	5.412	1.358	0.004
-1.329	1080.0	-4.698	8.89	5.384	1.409	0.003
-1.129	951.4	-4.947	8.61	5.353	1.451	0.002
-0.925	824.3	-5.220	8.37	5.321	1.488	0.002
-0.715	710.5	-5.499	8.18	5.287	1.518	0.001
-0.507	616.0	-5.764	8.02	5.253	1.544	0.001
-0.301	535.4	-6.022	7.88	5.220	1.566	0.000
-0.097	464.3	-6.283	7.76	5.188	1.585	0.000
0.114	404.0	-6.536	7.66	5.154	1.601	0.000
0.326	351.7	-6.788	7.56	5.121	1.617	0.000
0.540	305.5	-7.042	7.48	5.086	1.630	0.000
0.740	267.8	-7.280	7.41	5.053	1.642	0.000
0.942	235.0	-7.515	7.34	5.020	1.653	0.000

Table 1d. Evolution of a $0.04 M_{\odot}$ ($42 M_J$) Brown Dwarf

$\log t$ (Gyr)	T_{eff} (K)	$\log L/L_{\odot}$	R (10^9 cm)	$\log T_c$ (K)	$\log \rho_c$ (g cm^{-3})	L_{nuclear}/L
−2.982	2847.0	−1.812	35.48	5.777	0.347	0.439
−2.780	2857.0	−1.850	33.73	5.795	0.408	0.900
−2.573	2860.0	−1.864	33.13	5.801	0.430	0.943
−2.372	2866.0	−1.886	32.16	5.812	0.466	0.909
−2.172	2881.0	−1.962	29.16	5.847	0.586	0.632
−1.967	2883.0	−2.287	20.04	5.977	1.061	0.000
−1.765	2842.0	−2.537	15.47	6.058	1.397	0.000
−1.557	2774.0	−2.754	12.64	6.110	1.660	0.000
−1.357	2677.0	−2.957	10.75	6.138	1.871	0.000
−1.155	2537.0	−3.171	9.35	6.146	2.052	0.000
−0.948	2340.0	−3.414	8.31	6.134	2.207	0.000
−0.743	2035.0	−3.736	7.58	6.103	2.327	0.000
−0.537	1635.0	−4.164	7.18	6.070	2.397	0.000
−0.331	1451.0	−4.404	6.91	6.037	2.447	0.000
−0.125	1296.0	−4.630	6.67	5.998	2.493	0.000
0.077	1127.0	−4.900	6.47	5.954	2.532	0.000
0.278	968.6	−5.184	6.32	5.911	2.564	0.000
0.487	820.7	−5.490	6.19	5.867	2.590	0.000
0.699	680.9	−5.828	6.09	5.828	2.609	0.000
0.903	586.2	−6.098	6.02	5.794	2.624	0.000
1.113	511.7	−6.344	5.96	5.758	2.638	0.000

Table 2. Absolute Magnitudes of Synthetic BD/EGPs, $[M/H]=0.0$ [†]

g (cm s ⁻²)	T_{eff} (K)	M_J	M_H	M_K	$M_{L'}$	M_M	M_N
10^5	1000.0	15.35	14.99	15.62	13.34	12.56	12.51
	800.0	16.44	16.01	17.09	14.13	13.14	13.29
	600.0	17.91	17.40	19.27	15.18	13.94	14.21
	500.0	18.96	18.39	20.96	15.94	14.49	14.77
3×10^4	1000.0	14.96	14.52	14.98	12.99	12.12	12.03
	800.0	16.04	15.54	16.40	13.83	12.71	12.83
	600.0	17.49	16.92	18.43	14.94	13.51	13.78
	400.0	20.33	19.69	22.97	16.97	14.96	15.04
	300.0	22.62	21.91	26.74	18.58	16.08	15.74
10^4	1000.0	14.66	14.11	14.26	12.70	11.70	11.57
	800.0	15.82	15.23	15.88	13.66	12.39	12.49
	600.0	17.27	16.61	17.89	14.84	13.24	13.50
	400.0	19.76	19.31	21.86	16.74	14.64	14.71
3×10^3	1000.0	13.97	13.15	13.05	12.31	11.16	10.95
	800.0	15.42	14.64	15.00	13.38	11.97	12.07
	600.0	17.17	16.48	17.44	14.72	12.97	13.21
	400.0	19.84	19.40	21.49	16.77	14.49	14.54
	200.0	24.60	24.03	28.84	19.93	16.58	15.91

[†]We employed the transmission curves of Bessell & Brett (1988) and Bessell (1990) to define the photometric bandpasses and the model of Vega by Dreiling & Bell (1980) for the calibration of the magnitude scale.

Table 3. Color Indices of Synthetic BD/EGPs, $[M/H]=0.0$

g (cm s $^{-2}$)	T_{eff} (K)	$J - H$	$J - K$	$H - K$	$K - L'$	$M - N$
10^5	1000.0	0.35	-0.28	-0.63	2.28	0.05
	800.0	0.43	-0.65	-1.08	2.96	-0.15
	600.0	0.51	-1.36	-1.87	4.09	-0.27
	500.0	0.57	-2.00	-2.57	5.02	-0.27
3×10^4	1000.0	0.44	-0.02	-0.46	1.99	0.09
	800.0	0.50	-0.37	-0.87	2.58	-0.12
	600.0	0.57	-0.94	-1.51	3.49	-0.27
	400.0	0.63	-2.64	-3.27	5.99	-0.08
	300.0	0.71	-4.12	-4.83	8.17	0.34
10^4	1000.0	0.55	0.40	-0.15	1.55	0.13
	800.0	0.59	-0.06	-0.65	2.22	-0.10
	600.0	0.66	-0.62	-1.28	3.05	-0.26
	400.0	0.46	-2.10	-2.56	5.12	-0.08
3×10^3	1000.0	0.82	0.92	0.10	0.74	0.21
	800.0	0.78	0.42	-0.36	1.62	-0.10
	600.0	0.69	-0.28	-0.97	2.73	-0.24
	400.0	0.45	-1.65	-2.10	4.73	-0.05
	200.0	0.56	-4.25	-4.81	8.91	0.67